Materials Science & Engineering R 159 (2024) 100803

Contents lists available at ScienceDirect

Materials Science & Engineering R

journal homepage: www.elsevier.com/locate/mser

Ultraviolet photoluminescent materials from traditional ion-activated phosphors to emerging carbon dots and perovskites

Mingxue Deng [a], Yanjie Liang [b], Yun Shi [a], Jiacheng Wang [c], Junfeng Chen [a,*], Qian Liu [c,*]

[a] Shanghai Institute of Ceramics, Chinese Academy of Sciences, Shanghai 201899, China
[b] Shandong University, 17923 Jingshi Road, Jinan 250061, China
[c] State Key Laboratory of High Performance Ceramics and Superfine Microstructure, Shanghai Institute of Ceramics, Chinese Academy of Sciences, Shanghai 201899, China

ARTICLE INFO

Keywords:
Ultraviolet photoluminescent materials
Ion-activated
Phosphors
Carbon dots
Perovskites

ABSTRACT

Since Niels Ryberg Finsen won the Nobel Prize 120 years ago for his invention of ultraviolet (UV)-based phototherapy for skin tuberculosis (lupus vulgaris), UV has made great strides, benefit from its powerful sterilization function in the face of the global novel coronavirus epidemic more than 100 years later. Nevertheless, the development of high-efficiency UV materials and devices has encountered tremendous challenges and lags behind comparable visible light-emitting products. Due to the diversity of UV luminescent materials, the field of chemistry is still incomplete, which means that much fundamental knowledge remains to be discovered. In the early days of the exploration of UV photoluminescent materials, rare earth or main group metal ion-activated phosphors are one of the main candidates because of their simple synthesis methods. Recently, carbon dot-based nanomaterials as well as perovskite nanocrystals have been shown to achieve narrow band and high quantum yield. In this review, we systematically review aspects covering the development history, design principles, classification and applications of all promising UV photoluminescent materials, which may inspire researchers to explore the great potential of the UV region.

1. Introduction

In 1903, Danish scientist Finsen was awarded the Nobel Prize in Physiology and Medicine for his contributions to the treatment of lupus vulgaris with high doses of ultraviolet (UV) radiation. UV luminescent materials are a kind of electromagnetic radiation with high energy (200–400 nm) that has attracted extraordinary attention in commercial, civil and military fields. [1] UV is composed of three regions: UVC (200–280 nm), UVB (280–320 nm), and UVA (320–400 nm) according to their emission wavelength. Up to date, material systems and display lighting devices in visible light (red, green, blue) band have been developed relatively mature and perfect. However, the research and development of high efficiency UV light-emitting materials and devices products is relatively lagging behind. In our view, the evolution of UV material chemistry involves three distinct phases (Fig. 1**a**): (I) the discovery phase (1877–1990), (II) the initial development phase (1990–2005), and (III) the explosive development phase (2005–present).

The milestones in the development of UV luminescent materials are shown in Fig. 1**b**. In the 1900 s, Finsen's invention of an arc lamp with UV emission gave a ray of hope to patients with unusual lupus, making phototherapy an official medical treatment. With the development of emerging technologies, the combination of $BaSi_2O_5$:Pb^{2+} or SrB_4O_7:Eu^{2+} UV emission phosphors with low pressure mercury lamps has played an important role in photocopying, phototherapy, and tanning. [2] Currently, UV LEDs composed of carbon dots can achieve a photoluminescence quantum efficiency (PLQY) of 63%. [3] In contrast, the groundbreaking work on graphene quantum dots reported by Tang et al. in 2012 had only 7–11% PLQY. [4] Later, with the development of synthesis techniques, quantum dots in the UVB region were realized. In recent years, rare earth ions activated inorganic oxides have also achieved persistent luminescence (PersL) in the UVC region for more than 12 hours. [5] And perovskite nanocrystals appear with high purity and high efficiency, achieving PLQY of $>$ 95%. [6] Each UV light with a specific wavelength plays an irreplaceable role in industry and medicine, including phototherapy, antibacterial or purification, plant lighting, LED, as well as anti-counterfeiting (Fig. 1**c**).

Although there have been reviews of UV materials in recent years,

* Corresponding authors.
E-mail addresses: jfchen@mail.sic.ac.cn (J. Chen), qianliu@mail.sic.ac.cn (Q. Liu).

https://doi.org/10.1016/j.mser.2024.100803
Received 8 December 2023; Received in revised form 27 April 2024; Accepted 2 May 2024
Available online 10 May 2024

especially in PersL and electroluminescence, a comprehensive discussion of all UV photoluminescent materials, emphasizing the multiple types of UV luminescent materials, their transition luminescent mechanisms, and promising applications, is lacking. To the best of our knowledge, two overview work on Pr^{3+} ion-activated UV PersL materials as well as other ion-activated UV PersL materials was conducted by Mao et al. [7,8] The discussion deals with UV PersL properties of conventional inorganic oxide materials such as Pb^{2+}, Gd^{3+}, Ce^{3+}, Bi^{3+}, and Pr^{3+}-actived materials. However, as the new coronavirus dominates the global agenda, the development of efficient, low-cost and non-toxic UV LED opens up a new technological pathway for sterilization and water treatment, which has aroused strong interest among researchers. Recently, UV has been increasingly applied in the fields of phototherapy and plant lighting, and the types of materials have expanded from traditional phosphors to the emerging perovskite nanocrystals and carbon dot-based nanomaterials.

This paper first introduces the luminescence principles, design strategies and challenges of different UV materials, including (i) rare earth or main group metal ion-activated phosphors; (ii) carbon dot-based nanomaterials; (iii) perovskite nanocrystals. Then the performance of UV luminescent materials and related devices is highlighted. In addition, their applications in different scenarios are summarized. Finally, we describe current challenges and suggest potential ways to overcome them, building on the breakthroughs achieved with UV luminescent materials in the past few years. We hope that this review provides an effective framework for addressing the challenges currently hindering the applications of UV-emitting materials, thereby facilitating the emergence of innovation. There is no doubt that innovative synthesis techniques and the development of novel materials will facilitate the discovery of superior performance and subsequent applications of UV-emitting materials for the benefit of society as a whole.

2. Design principles of UV photoluminescent materials

The performance breakthrough of UV photoluminescent material system relies on more systematic and comprehensive conformational research and design strategy. Initially, rare earth or transition metal ion-activated phosphors became the most intensively studied UV luminescent materials due to their variable and controllable chemical components as well as dopant ions and simple synthesis strategies. In addition, carbon dot-based nanomaterials and perovskite nanocrystals also grow into latecomers of UV luminescent materials because of their composition tunability and high color purity, and receive more and more attention.

These 3 types of materials have similarities and differences in their luminescence mechanisms involving carrier and exciton dynamics

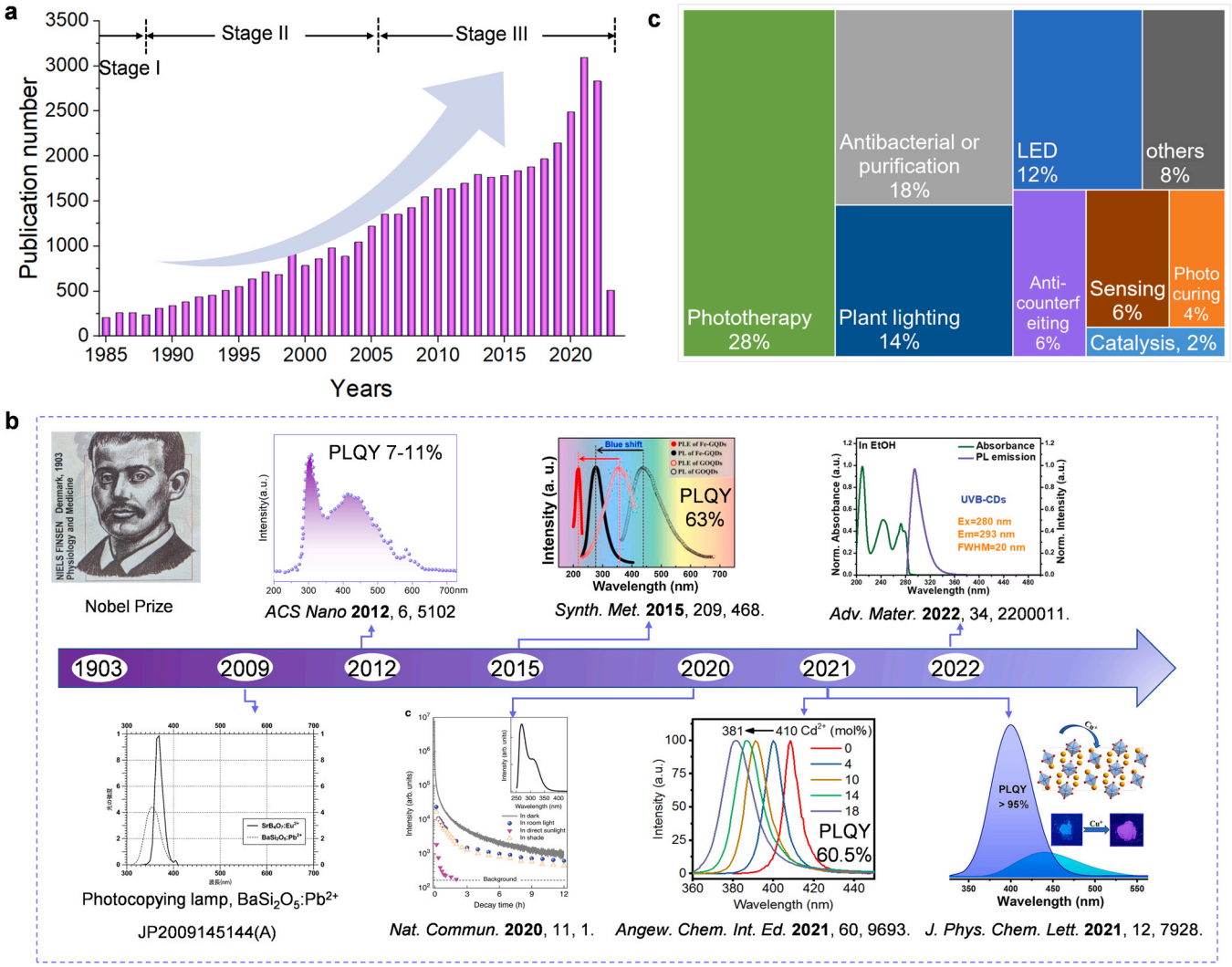

Fig. 1. The developmental lineage of UV-emitting materials chemistry. a. The histogram of the number of publications on UV-emitting materials. **b.** Timeline for the development of UV-emitting materials. **c.** Schematic representation of the percentage of UV-emitting materials in various application. Data from Web of Science from 1958 to 2023.

processes. Inspired by the promising properties, the fundamental optical performance and optimization strategies of the above 3 types of UV materials have been explored extensively. Nevertheless, it is still challenging to design and develop efficient UV luminescent materials.

2.1. Basic principle of rare earth or main group metal ion-activated phosphors

Typical inorganic oxide UV phosphors are mainly composed of matrix lattice and activator (luminescent center). Various rare-earth ions or

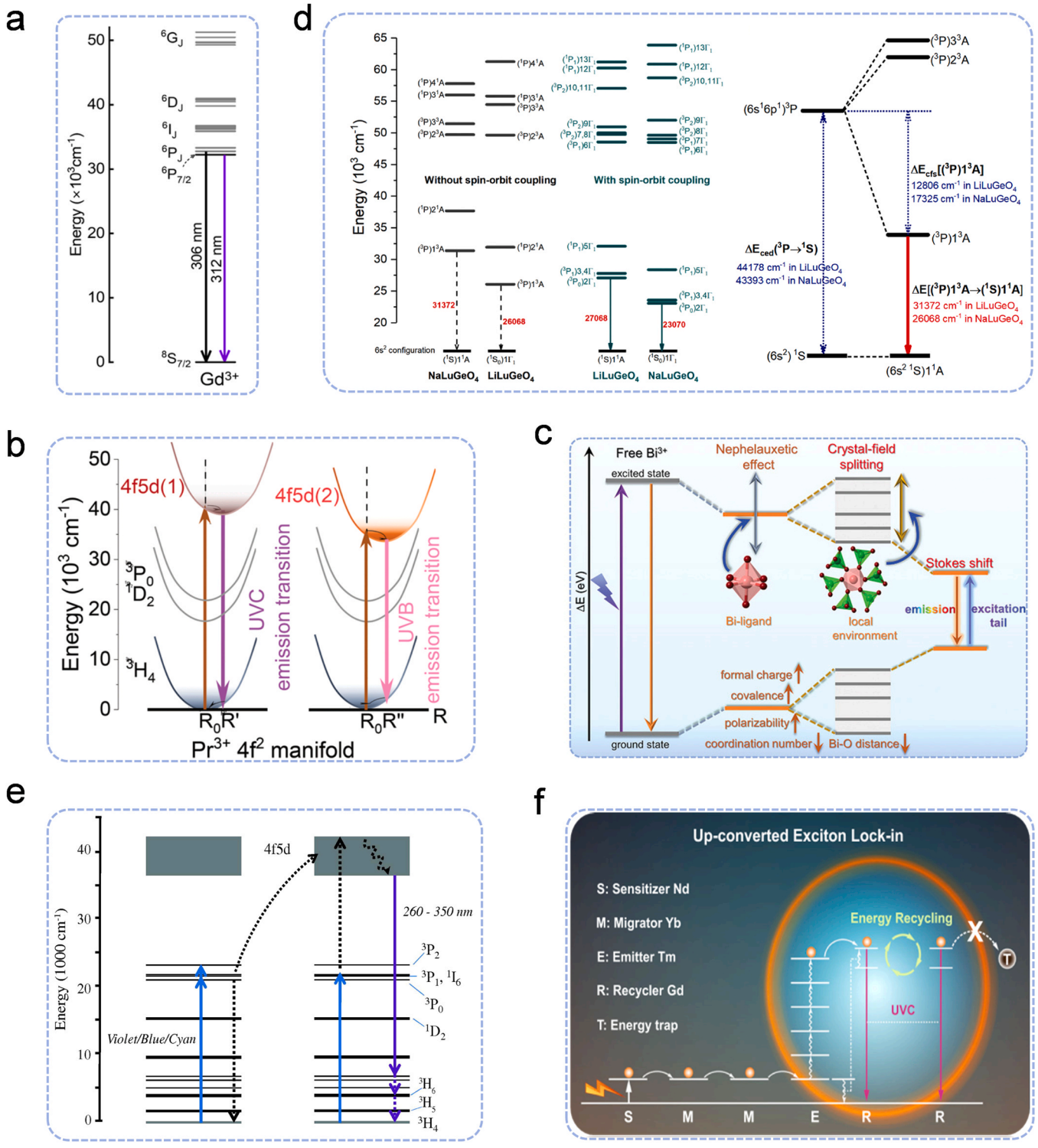

Fig. 2. Basic principle of rare earth or main group metal ion-activated UV phosphors. a. Energy level scheme of Gd^{3+} ion in $Sr_2P_2O_7$ phosphor [9]. Copyright 2022. **b.** Configurational coordinate diagrams of Pr^{3+} for possible 4f5d energy states [12]. Copyright 2022. **c.** Energy level diagram of free Bi^{3+} ions and influencing factors of Bi ion emission [13]. Copyright 2021. **d.** Calculated electric structure of Bi^{3+} $6s^16p^1$ configuration in $ALuGeO_4$ (A= Li, Na) [14]. Copyright 2019. **e.** Schematic diagram of Pr^{3+} upconversion from visible-to-UV [15]. Copyright 2018. **f.** Diagram of six-photon up-conversion excitation lock-in for UV enhancement [16]. Copyright 2023.

main-group metal ions in a suitable lattice will produce UV emission. Since the activators or luminescent groups in the matrix lattice are sensitive to external optical stimuli, such as ultraviolet light, high-energy electron beams, or X-rays, the electron separates from the hole. The electron is promoted to a higher excited state or conduction band (CB), and the hole jumps to the valence band (VB). One part of the carriers undergoes non-radiative relaxation loss. Another part of the electrons in the excited state immediately recombine with holes, releasing low-energy photons and achieving UV photoluminescence [8.]

2.1.1. Photophysics of the UV emission from 4 f to 4 f transition RE^{3+} ions

Optically active lanthanide rare earth ion RE^{3+}, whose 4f orbital not being completely filled, has an external electron configuration of 5 s^2 5p^6 4f^n (n is any integer from 1 to 13). Located in the interior of the ion, this 4f orbital is shielded by the less energetic 5 s^2 and 5p^6 orbitals on the periphery. Despite the importance of the matrix lattice, it has little effect on the 4f^n configuration. For rare earth free ions, the electric dipole interaction cannot cause 4f–4 f transition. Therefore, transitions between energy levels in the 4 f^n configuration are spin-forbidden. That is, the optical absorption transition in the rare earth ion 4 f^n configuration is strongly restricted by the parity selection law.

When the crystal lattice occupied by rare earth ions does not have inverse symmetry, the non-even terms of the corresponding crystal field are more important. At this point, these non-even terms can cause a small number of opposite parity wave functions (such as 5d) to mix with the 4 f wave function. In this way, the strength of the transition between the 4f^n configurations is increased.

Gd^{3+} is a typical UV emission activator for the narrow band f-f transition, originating from the $^6P_{7/2}\rightarrow{}^8S_{7/2}$ transition. Unlike other activators, the excited states of Gd^{3+} are all high above 30,000 cm^{-1}, which creates a high energy barrier for UV emission **(**Fig. 2**a)**. However, Gd^{3+} has a semi-filled 4 f^7 configuration that is difficult to oxidize or reduce. Thus, it is hard to effectively excite Gd^{3+} ion utilizing the UV light with shorter and broadband wavelength. [9] Considering that their excited states (i.e. the 4f 5d excited states of Pr^{3+} and Ce^{3+}, the $^3P_1$ emission states of Bi^{3+} and Pb^{2+}) overlap with the $^6I_J/^6P_J$ states of Gd^{3+}, highly efficient narrowband-UVB (NB-UVB) luminescence can be achieved by introducing a suitable sensitizer, like Bi^{3+}, Pr^{3+}, Ce^{3+} and Pb^{2+} ions, to transfer energy to Gd^{3+}. [10,11] This strategy enables intense NB-UVB emission of Gd^{3+} ions in the range of 310 – 313 nm.

2.1.2. Photophysics of the UV emission from 4 f to 5d transition RE^{3+} ions

The UV luminescence of rare earth ions in solids has a class of band spectra in addition to the aforementioned 4f–4 f line spectra. Band spectra are the transition between the energy levels in the 4f^n configuration and other 4f^{n-4} f^{n-1}5d configuration levels, i.e., the 4 f-5d transition. However, the 4 f-5d transition is spin-allowed. The 4 f-5d transition ion has the significant advantage of a short decay lifetime compared to the traditional f-f transition with a lifetime of up to milliseconds. The typical lifetime is below the nanosecond level, which greatly reduces excited state quenching, resulting in higher brightness. [17] Not only that, the emission wavelength is able to be tailored by regulating the coordination environment. Since the 5d orbital is sensitive to the ligand field, while the 4 f orbital is insensitive to the surrounding environment under the effective shielding of 5s5p. [18]

The trivalent Pr^{3+} is a typical f-d transition ion that produces efficient UV emission due to its characteristic 4 $f^1$5$d^1\rightarrow$4 f^2 inter-configuration energy transition mechanism. However, the non-radiative relaxation of the 4 $f^1$5d^1 energy level of Pr^{3+} minimized to the lower 4 f^2 energy level (^3P_j, $^1I_6$, $^1D_2$) can cause efficient UV emission only if the first (lowest energy) 4 $f^2\rightarrow$4 $f^1$5d^1 excitation transition is at a suitable energy position and the Stokes shift is less than about 3000 cm^{-1}, as shown in Fig. 2**b**. [5] Otherwise, the 4 $f^1$5d^1 level will cross with the lower 4 f^2 level, resulting in the emission of sharp spectral lines of visible and/or infrared light, i.e., the emission transition within the 4 $f^2\rightarrow$4 f^2 configuration will dominate. The splitting of 4f5d energy level is affected by Coulomb force, orbital spin and crystal field. The splitting degree of matrix crystal field leads to different splitting and displacement degrees of 5d energy level, resulting in different emission spectra of materials excited by high-energy light. The smaller the splitting degree, the bluer the emission spectrum moves to UV band.

The emission of Ce^{3+} comes from the transition between the lowest crystal field energy level in the $5d^1$ configuration and the two ground state levels, showing double-band emission. [19] And it is generally located in the UV to blue light, and a few can be extended to green and red light. The emission wavelength mainly relies on (1) the electron cloud expansion effect; (2) crystal field splitting in the $5d^1$ group state: the stronger low-symmetry crystal field, the lower the energy value of the lowest crystal field energy level; (3) the Stokes shift. By decreasing covalency and increasing the 4 f,5d energy level difference, the emission wavelength can be shifted to the UV region. However, the 5d energy level of Ce^{3+} ions often splits and the strong low-symmetry crystal field reduces the energy of the lowest 5d energy level.

2.1.3. Photophysics of the UV emission from ns^2 ions

The ions with the outermost s^2 configuration are important in the field of UV luminescence, and its electronic configuration is [Xe](n-2) f^{14}(n-1)$d^{10}ns^2np^3$. The main ions in this category with UV emission are Bi^{3+} and Pb^{2+}(6 s^2). Their sp configuration can produce a lower energy ^3P state with lower energy when excited. This energy state is subject to the interaction of spin-orbit coupling and Jahn-Teller coupling. These two coupling types also have a competitive relationship, when the spin-orbit coupling is strong, then the Jahn-Teller coupling effect will decline. The spin-orbit coupling can divide the ^3P state into three energy levels, $^3P_0$, $^3P_1$ and $^3P_2$. The intensity of spin-orbit coupling increases as the charge number changes from low to high. In the 6 s^2 ion, the spin-orbit coupling is so strong that the emission spectra can be directly based on the $^3P_0$ and $^3P_1$ energy levels obtained by spin-orbit splitting.

Taking a typical Bi^{3+} as an example, the exposed 6 s^2 electrons of Bi^{3+} are extremely sensitive to the crystal field of the host. [20] The emission peak of Bi^{3+}-doped oxide is greatly affected by the crystal field splitting, coordination number, fractional covalent character, and formal charge **(**Fig. 2**c)**. [13] And the weaker crystal field of the host leads to an increase in the energy of the $^3P_0\rightarrow{}^1S_0$ transition and a blue shift in the emission wavelength. Since the luminescence of $^3P_0\rightarrow{}^1S_0$ is strongly spin-forbidden at low temperatures, the luminescence decay time becomes very long (ms level). However, electrons begin to heat up in the $^3P_1$ energy level at higher temperatures, and the decay time is also greatly accelerated. [19]

First-principles calculations to obtain the electronic structure of Bi^{3+} can help us gain insight into the underlying microscopic mechanisms and predict luminescence properties.[21,22] The emission of $ALuGeO_4$: Bi^{3+} (A = Li, Na) redshifts from 360 nm to 418 nm after the replacement of Li^+ by Na^+. Wang et al. used first-principle calculations to find that the redshift of emission is due to the crystal field effect caused by the different excited-state local structures of Bi^{3+} (Fig. 2**d**). [14] The calculated Debye temperature and vibrational frequency indicate that the local structural stiffness around Bi^{3+} decreases from A = Li to Na, which is responsible for the larger local structural distortion after the 6 s→6p excitation of Bi^{3+}.

2.1.4. Upconversion mechanism

Most of the above photoluminescence processes follow Stokes law, i.e., the emission always has a lower energy and a longer wavelength. [23] In contrast, upconversion (UC) of anti-Stokes emission is excited by low-energy light and can emit light of high energy and short wavelength. Cheng et al. provide a detailed overview of the mechanisms of lanthanide-doped upconversion luminescence, including excited state absorption (ESA), energy transfer upconversion (ETU), cooperative sensitization upconversion (CSU), photon avalanching (PA), and energy migration-mediated upconversion (EMU). [24] The ESA mechanism, which utilizes the sequential absorption of two photons in the

intermediate excited state, and the ETU mechanism, which utilizes the resonance energy transfer excitation between two neighboring ions to the intermediate energy level, are the two simplest UC mechanisms occurring in UV inorganic phosphors.

Pr^{3+} activators are the most efficient approach achieving UV emission under visible light excitation, through ESA or ETU process involving 4f5d band emission, as depicted in Fig. 2**e**. [15,25,26] The 4f 5d level of Pr^{3+} ions must be low enough, which is an critical criterion for Pr^{3+} visible-to-UV emission. Hosts with low crystal field splitting leading to high energy 4f5d level locations, such as fluoride, do not possess such UC. [27] The ability of optically active ions to continuously absorb photons depends on the extremely long lifetime of the intermediate excited state ^3P_J (τ_i) to enhance the energy transfer between ions in these states. This allows for the capture of multiple photons over longer time scales, thus allowing for low-energy stimulation sources. The rate of nonradiative and radiative together determine the value of τ_i. Thus, it has been established that host with lower phonon energies (ideally $<600\ cm^{-1}$) is able to reduce the $^3P_0 \rightarrow {}^1D_2$ multi-phonon relaxation rate and the phonon-assisted $[^3P_0, {}^3H_4] \rightarrow [^1D_2, {}^3H_6]$ cross-relaxation. This leads to lower nonradiative decay rates and longer τ_i, which implies higher efficiency of the UC process. Low phonon energies can minimize the loss of nonradiative relaxation and maximize the radiative transition of the activator. Additionally, dispersing Pr^{3+} clusters can also alleviate cross-relaxation by co-doping with alkaline-earth metal ions Li^+, Na^+, and K^+, etc. [15,28]

However, the upconversion of near-infrared (NIR) to UV is not only affected by the inherent spin-forbidden of the 4 f−4 f optical transition in the lanthanide, but also significantly affected by numerous harmful factors such as concentration quenching, cross relaxation between lanthanide ions, surface quenching, and competitive energy harvesting induced by interior lattice defects. [29] Wei et al. have reviewed NIR to UV upconversion tuning strategies for lanthanide doped nanoparticles. [30] Su et al. proposed an upconversion excitation locking (UCEL) mechanism as shown in Fig. 2**f**. [16] The excitation energy of Gd^{3+} sensitization can be retained by simply using an intermediate layer in $NaYF_4$:Yb^{3+}, which is optically inert to the excited Gd^{3+}. This nanostructure retains the upconverted UV energy within the core region and effectively suppresses the energy dissipation of internal traps, resulting in a six-photon upconversion UVC emission at 253 nm under 808 nm excitation.

2.2. Mechanism of UV emission in carbon dot-based nanomaterials

The origin and mechanism of carbon dot-based nanomaterials (CDs) photoluminescence is the most important and challenging task in research. [31,32] It is worth noting that the self-absorption of CDs has little effect on emission, which favors UV emission. [33] In general, CDs are categorized into graphene quantum dots (GQDs), carbon quantum dots (CQDs), carbon nanodots (CNDs), etc. [34] Up to now, the main UV emission mechanisms of CDs include (1) quantum confinement effect mechanism (size effect)[35], (2) surface state mechanism[36], and (3) defect state mechanism [37], as depicted in Fig. 3. The molecular mechanism and cross-linked enhanced emission effect mechanism[38] have not been reported in UV emission, so we will not discuss them in this review.

2.2.1. Quantum confinement effect

The influence of quantum confinement effect, which is the most dominant mechanism for obtaining UV emission, can control the band gap. [39] The emission wavelength of CDs decreases with the expansion of its band gap. [40] Therefore, it is an effective strategy to shift the luminous blue to the UV band by widening the band gap. By electron confinement, CDs, which are semi-metallic in nature, can be converted into a semiconductor form with a finite band gap. In other way, the introduction of heteroatoms with low electronegativity doped into the sp^2 domain can expand its band gap.

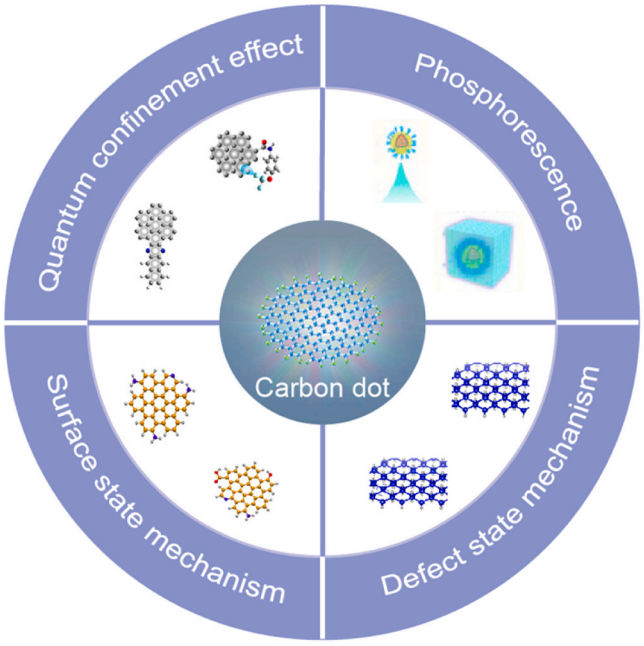

Fig. 3. UV emission mechanisms of CDs.

Shan et al. designed UV emission CNDs with wide band gap based on theoretical calculation. [41] DFT calculations showed that the band gaps between methyl red and the three configurations of o-, m-, and p-phenylenediamine (OPDA, MPDA, PPDA) were 4.47, 4.69 and 4.18 eV, respectively (Fig. 4**a**). Such a wide band gap provides sufficiently radiative transition paths for UVB emission. The emission wavelengths of CNDs in the range of 280 ~ 300 nm are realized, which are in good agreement with the theoretical calculations.

Yan et al. expanded the π-conjugated sp^2-carbon system by conjugating GQDs with polyaromatic groups leading to a narrowing of the band gap of GQDs from 2.40 to 1.94 eV, which in turn induced a redshift in the PL spectrum (Fig. 4**b**). [40] The band gap narrowing is mainly attributed to the lowering of the π* orbitals. Alternatively, the band gap is reduced by introducing intermediate orbitals between the π and π* orbitals after conjugation with an electron-donating functional group. However, such a narrow bandgap can only cause visible light emission rather than UV emission.

2.2.2. Surface state mechanism

Surface state mechanism is another effective strategy to obtain UV emission. PL properties of CDs are affected by oxygen-containing functional groups on the surface sites or edges, surface dangling bonds, or the formation of transient trap states. [42] It has been reported that they trap photogenerated charge carriers through large amplitude vibration and distortion, thereby reducing the PLQY.[45] Due to surface dangling bonds can capture electrons through non-radiative pathways, surface passivation facilitates the removal of surface dangling bonds.

Yuan et al. achieved high-colour-purity deep-blue CD LEDs (PLQY70% ± 10%) by efficient edge amine passivation (Fig. 4**c**). [42] This provides a solution for obtaining a UV emission scheme. In this way, Lau and co-workers obtained GQDs with a unique surface self-passivation layer by a microwave-assisted hydrothermal method, showing UV optical properties for the first time. [4] Ding et al. achieved UV emission and highest PL quantum yields (QY) of 63% in ferric passivated GQDs (Fe-GQDs) by surface passivation of Fe. [3]

2.2.3. Defect state mechanism

The structural domain composition of CDs is often accompanied by various defects in the non-perfect sp^2 structural domain, which exhibit multiple electronic transitions between the band gaps, resulting in

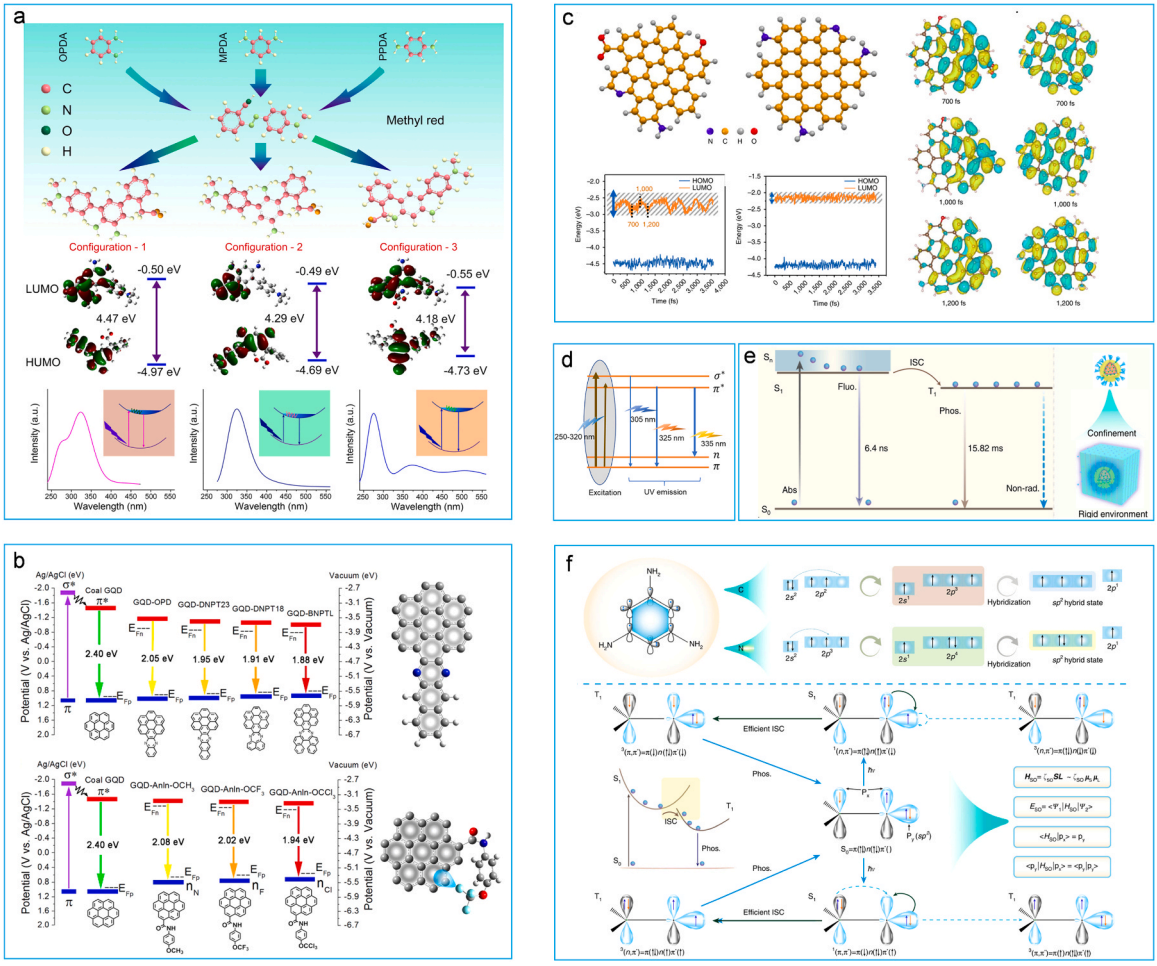

Fig. 4. The design principle for UV emission of CDs. **a.** Schematic diagram describing the effect of three configurations on the energy gap and spectra of CDs [41]. Copyright 2019. **b**. Energy level diagrams and simplified structural schematics [40]. Copyright 2018. **c.** DFT calculation of band gap vibrations of CDs with different terminal functional groups [42]. Copyright 2020. **d.** Model illustrating the excitation and emission of the CNDs [43]. Copyright 2021. **e.** A transition model of the UV fluorescence and phosphorescence in CND [44]. Copyright 2022. **f.** Schematic diagram of CNDs molecular structure units and electron orbitals and phosphorescence attenuation [44]. Copyright 2022.

narrow band gaps of CDs. [46] In general, the abundance of defective states in CDs affects their luminescence properties. However, it's so complicated of CDs' surface defects states that are associated with sp^2, sp^3 hybridized carbon and functional groups containing heteroatoms, dangling bonds and non-radiative states. [47]

On the one hand, CD surface defects lead to multicolor emission in the visible-UV spectral range. On the other hand, similar to the surface state, the existence of defect states will capture excited carriers, which further increases the difficulty of obtaining UV emission. Moreover, the stacked defects in the crystal structure suppress the efficient UV emission. Kim et al. eliminated stacking defects in the crystal structure of ZnSe QDs by adding hydrofluoric acid and zinc chloride additives, achieving near-unity quantum yields. [45]

Recently, Bi et al. used a sp^3 bonding strategy to achieve UV emission. [48] The sp^2 structural domains are well delineated spatially by sp^3 structural domains, greatly reducing the quenching effect caused by aggregation. In addition, Shi et al. obtained broadband UV emission using a pulsed laser ablation method to eliminate defects and surface trapping of excited electrons. [43] Specifically, the three UV emission bands located at 305 nm, 325 nm and 335 nm are attributed to the $\sigma^*\rightarrow\pi$, $\pi^*\rightarrow\pi$, and $\pi^*\rightarrow n$ transitions, respectively (Fig. 4**d**).

2.2.4. *Phosphorescence mechanism*

In recent years, there has been great interest in the phosphorescence of CDs. [49] Phosphorescence, of which lifetime is generally longer than that of the fluorescence, is the radiative transition from the triplet state (T_1) to the single-linear ground state (S_0). In general, CDs rarely exhibit phosphorescence thanks to the instability of their triplet excited states.

The triplet excited state of CDs is mainly stabilized by constructing a CDs hybrid system in an organic or inorganic matrix, so that CDs can produce typical phosphorescent emission. [50] The triplet excited states of CDs can be protected from rotational or vibrational losses through hydrogen bonds formed with organic substrates such as polyvinyl alcohol. Furthermore, covalent bonds with stronger interactions can serve as a more efficient alternative to immobilize and rigidify triplet emitting species. Therefore, the researchers attempted to bind CDs into inorganic substrates, like SiO_2, by covalent bonding. [51] In addition, CDs embedded in the discontinuous nanospace or attached to the outer surface of the zeolite host can produce a structural confinement effect on CDs, resulting in phosphorescence. [52]

However, there is an emission wavelength limitation to the phosphorescence of CDs, with the vast majority concentrated in the visible region. It is highly promising and challenging to explore CDs with long-life, high-efficiency phosphorescence. Shan et al. proposed the manufacturing strategies for UV phosphorescent CDs: (1) Smaller conjugate size to increase the system energy to obtain short wavelength emission. (2) Heteroatoms containing lone pairs of electrons to provide enough intersystem crossing (ISC) driving force. (3) In situ confinement

environment to reduce the energy dissipation path of the resulting triple exciton. [44] Fig. 4**e** depicts the transition of phosphorescence centered at 348 nm and a lifetime of 15.8 ms obtained by this method. The simple preparation process, wide size tuning range and abundant surface passivation/modification strategies of CDs make them very promising UV-emitting active materials with fascinating optical properties for both fluorescence and phosphorescence (Fig. 4**f**).

2.3. Photophysics of perovskite nanocrystals

The structure/composition diversity and tunable band structure of perovskite nanocrystals provide suitable active sites and coordination environment for UV emission mechanism. There are three main UV emission mechanisms in perovskite nanocrystals: (1) emission of local atom-like states (intrinsic emission); (2) free exciton emission; (3) Self-trapping exciton emission.

2.3.1. Intrinsic emission

Intrinsic emission is the most common UV emission mechanism in metal halide perovskites (Fig. 5**a**). Intrinsic emission, that is, centered on metal cations, mostly involves lone pair electron ns^2 orbitals (e.g., Pb^{2+} or Hf^{2+}). For emerging metal halide perovskites, photoelectronic properties are greatly affected by lone-pair ns^2 electrons. [53] Taking a typical Pb^{2+} cation as an example, the lone-pair state $6s^2$ electron configuration is embedded in a mixed covalent-ion bonding lattice, which gives the lead halide perovskite outstanding photoelectric properties. What's more important, the emission and absorption spectra of Pb^{2+} in many host lattices are in the UV region. The energy level diagram of the free Pb^{2+} ion depicts that the ground state is $^1S_0$, and the excited states are triplet and single states ($^3P_{0,1,2}$ and $^1P_1$). [54] Due to the presence of lone-pair electrons, ns^2 ions tend to occupy off-center positions, leading to a larger Stokes shift. [55]

The s^2 ion effect, also known as the Jahn-Teller effect, has an important effect on the Stokes shift. It is mainly due to the deviation of the ground state ion from its central position caused by the lone-pair of electrons. In a soft lattice environment, electrons excited at the ion emission center of the ns^2 electron configuration strongly couple with the lattice. It is the electron-phonon coupling effect that produces broadband emission. Upon excitation, the lattice recombines with the help of Jahn-Teller deformation, which provides a trapping center for excitons.

Another factor affecting Stokes shift involves the charge transfer state, usually denoted as the D-state. With or without thermal activation, there is a transfer from the $^3P_{0,1}$ excited state to an excited state involving the matrix lattice. [60] This will produce a larger Stokes shift. The appearance of D-state relies on the size of the cation displaced by the Pb^{2+} ion and the effect of the electronegativity of the ligand. The recent Cs_4PbBr_6 provides an example for such cases. [56] There are two types of luminescence, in which the small Stokes shift emission at approximately 350 nm to the spin-orbit coupling allowed $^3P_1$ to $^1S_0$ transition in Pb^{2+} ions and the larger Stokes shift emission at approximately 400 nm to the D-state. DFT calculations show that once a Pb^{2+} ion from the Cs_4PbBr_6 lattice replaces a Cs^+ atom, an intra-gap energy level (D-state) originating from the Pb^{2+} ion appears at a position near the bottom of the CB (Fig. 5**b**). By coupling the D-state to the octahedron' vibrations in the matrix lattice, excited electrons can be transferred from the $[PbBr_6]^{4-}$ excited state energy level to the D-state of the Pb^{2+} ion.

Except for intrinsic emission of Pb^{2+} ion, Arnold Burger et al. reported that a broad band UV emission at about 400 nm in Cs_2HfCl_6 crystals is caused by D-state transition of the unperturbed $[HfCl_6]^{2-}$ anionic polyhedron, located in a cubic cavity formed by Cs^+ ions. [61] Saeki et al. [62] and Liu et al. [63] have also found the same phenomenon in Cs_2HfCl_6 nanocrystals.

2.3.2. Free excitons

The emission of free excitons (FEs), as a kind of emission mechanism widely existing in semiconductors, has attracted wide attention due to its high quantum efficiency and novel chemical and physical properties (Fig. 5**c**). The UV-emitting bands of typical 0D Pb-Br perovskites are narrow with small Stokes shift, which is generally considered to be a radiative emission of FEs. [64] FEs emission is a phenomenon where excited electrons and holes are bound together by Coulomb forces to form excitons and then recombine to emit light. And the exciton binding energy (E_b) is the magnitude of gravitational force between electrons

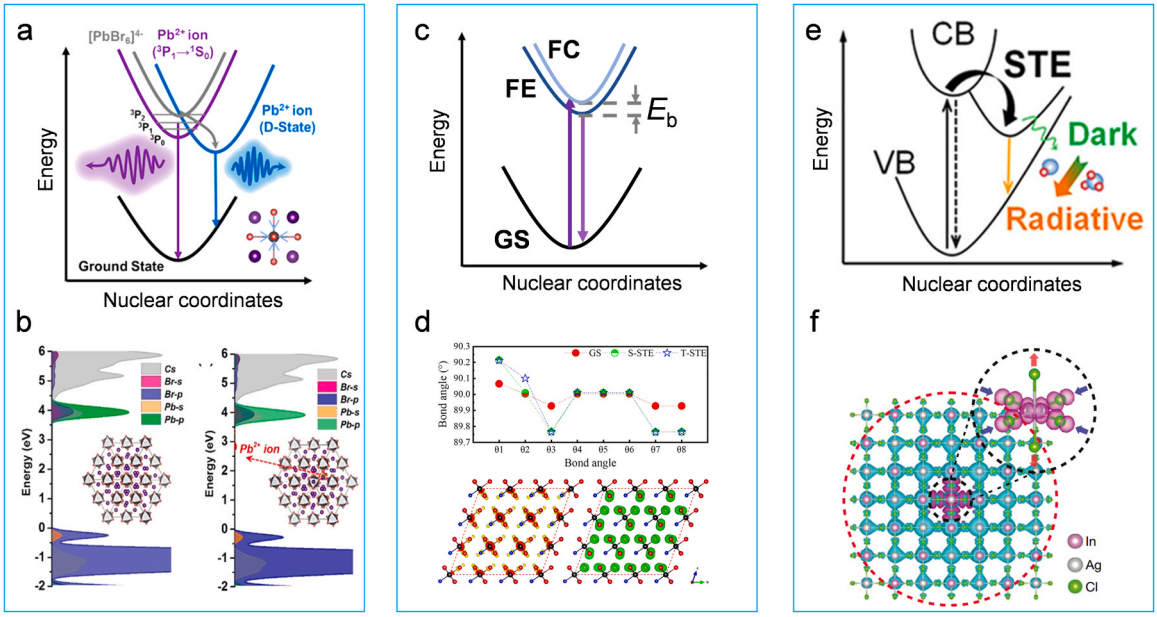

Fig. 5. Photophysics of perovskite nanocrystals. **a.** Intrinsic emission of Pb^{2+} ion [56]. Copyright 2017. **b.** Projected density of states Cs_4PbBr_6 supercells before and after the substitution of Cs with Pb^{2+} ion [56]. Copyright 2017. **c.** UV emission from free excitons. **d.** Bond angle (up), electron-associated (left), and hole-associated (right) partial charge densities comparison for GS, singlet-STE, and triplet-STE.[57] Copyright 2023. **e.** Energy level transition of STE [58]. Copyright 2022. **f.** DFT calculation of STE in $Cs_2AgInCl_6$ [59]. Copyright 2018. (FC means free carriers; FE means free excitons; GS represents ground state) An up arrow means excitation, and a down arrow means emission.

and holes. The increase of E_b helps to reduce the probability of exciton dissociation and enhance radiative decay rate of the exciton, thus improving the fluorescence efficiency. Gao et al. determined that partial substitution of iodine for bromine in $Cs_2Sn(Br_{1-x}I_x)_6$ leads to major FE emission through DFT calculations (Fig. 5**d**). [57]

The synergistic effect of quantum and dielectric confinement results in large E_b (≈320 meV) in two-dimensional (2D) perovskite. [65] In general, PL from free excitons under UV excitation is narrow-band emission with small Stokes shift. [66] Even at room temperature, clear exciton features are observed in low-dimensional hybrid perovskites. [67] Ishita Neogi et al. discovered a 2D hybrid organic–inorganic perovskite (CyBMA)$PbBr_4$ with a high exciton binding energy of 340 meV. [68] It shows a sharp dominant UV exciton peak and a less intense broad peak. Dominant exciton peaks are mainly derived from 2D hybrid organic–inorganic perovskite of non-luminous chromophores. However, PL shows strong electron-phonon coupling effect and wide-band emission at room temperature, and its narrow band UV exciton peak only appears at low temperature of 10 K in 2D perovskite $(C_6H_5C_2H_4NH_3)_2PbCl_4$. [69] There are three peaks located at 341, 347, and 350 nm for the dipole-allowed singlet exciton Γ_5^- and the dipole-prohibited triplet excitons Γ_2^- and Γ_1^-, respectively.

The smaller the dielectric constant and size of the material, the larger the exciton binding energy. Specifically, the quantum confinement effect in 2D perovskite lead to a fourfold enhancement of E_b over comparable 3D materials because the inorganic layer restricts the wave function of excitons to the two dimensions. [70] E_b is further enhanced by the shield of the organic layer from the attraction between electrons and holes, i.e., dielectric confinement effect. [71] It is the high dielectric confinement in 3D Pb-I lattice that shields the coulomb attraction between the excited electrons and the holes, resulting in a lower E_b. Additionally, Matthew et al. reduced dielectric limitation in layered perovskite by intercalation strategy. [72] This radiation recombination of weakly coupling electron-hole pairs typically results in small Stokes shifts and narrow half-peak widths of the PL spectrum.

2.3.3. *Self-trapping exciton emission*

Self-trapping exciton emission (STEs, Fig. 5**e**), which is widely found in metal halide perovskites, is a special kind of excitons luminescence. Luo et al. studied STE emission in $Cs_2AgInCl_6$, which attracted a lot of attention (Fig. 5**f**). [59]In a matrix with strong electron-phonon coupling, the carrier of the excited state interacts with the lattice leading to lattice distortion and the formation of highly localized STEs, which subsequently recombine to produce large Stokes shifts and efficient broadband emission. [59] The main reasons for the broadband emission characteristics of STEs are that the generation of lattice deformation energy during exciton self-capture leads to a partial loss of exciton energy when the ground state energy rises, resulting in an emission energy much smaller than the initial band gap. [73] In addition, the strong electron-phonon coupling is also the source of broadband.

Liu et al. observed extensive positive photo-induced absorption (PIA) in $Cs_4CuIn_2Cl_{12}$ double perovskite nanocrystals by ultrafast transient absorption spectroscopy (TA), providing direct evidence for UV emission originating from STEs. [58] The super-fast PIA signal growth (<1 ps) illustrates the transition from free excitons to STE trapping. [74] The TA spectra of moisture-assisted $Cs_4CuIn_2Cl_{12}$ nanocrystals exhibited a significant redshift, indicating that the STE effect was enhanced by the introduction of H_2O molecules.

The emission of STE in perovskite is closely associated with the distortion of the luminescence center and the structural dimension of the material. Mao L. et al. investigated that the bond length of the octahedra and the distortion of angular (β, δ) contribute to broadening of the PL emission in the $EA_4Pb_3Br_{10-x}Cl_x$ system. [75] During the evolution, $EA_4Pb_3Br_{10}$ is a narrow free exciton emission, while $EA_4Pb_3Cl_{10}$ is a broad STE emission. Smith M. D. et al. further found that the luminescence of STE was positively correlated with the degree of octahedral distortion in 2D perovskites, indicating that the larger the octahedral distortion, the more conducive to the generation of STE. [76] However, greater distortion often means that there may be more defects in the material, leading to enhanced phonon-assisted nonradiative composite paths and reduced fluorescence efficiency. [77] This may also be one reason why the maximum efficiency of 2D perovskite-like materials is only 9% of that of (EDBE)$PbBr_4$.

The dimension of the material is reduced from 2D to 1D and then to 0D, and the PLQY is significantly improved. [77] On the one hand, low structural dimension makes excitons strongly confined, which increases E_b and reduces the possibility of exciton dissociation. On the other hand, low structural dimension increases the effective mass of carriers, increasing the possibility of FE formation. The interaction with the relatively "soft" lattice of perovskite increases the possibility of STE formation. [73,78]

2.3.4. *Defective state*

Except for the above UV luminescence mechanism, surface passivation and adjustment of octahedral unit distortion can improve UV luminescence efficiency. In the case of $CsPbCl_3$, its low UV PLQY is considered to be a defective state caused by the chlorine vacancy and the distortion of the octahedral unit. The introduction of Cs^+ will cause the octahedral distortion. Therefore, a reasonable choice of smaller divalent cations to replace Pb^{2+} can reduce the vertical voids, thus reducing the tilt of the octahedral element and increasing the tolerance factor.

Theoretical studies have shown that Ni^{2+} doping perovskite increases the defect formation energy and improves the UV PLQY. [79] A recent study did also confirm the suppression of Cl vacancies and the reduction of octahedral distortion by Ni^{2+} doping. [80] Navendu Mondal et al. achieved blue-violet (PL peak position at 406 nm) PLQY to near unity by removing the non-radiative defect states in $CsPbCl_3$ nanocrystals with $CdCl_2$-treated. [81] Zhang et al. regulated the band gap of $CsPbCl_3$ nanocrystals by doping Cd^{2+}, resulting in the luminescence peak blue shift to the UV region of 381 nm. [82] What's more, PLQY was improved to 60.5% by $CdCl_2$ modification of the surface structure.

3. Rare earth or main group metal ion-activated UV phosphors

3.1. *Gd^{3+}-activated phosphors*

Gd^{3+} ion is a typical NB-UVB activator with strong emission in the range of 310 ~ 316 nm. Table 1 summarizes Gd^{3+}-activated UV luminescence materials. Gd^{3+} ion displays a very stable ground state of $^8S_{7/2}$, whose emission wavelength is almost unaffected by the crystal field. Singh et al. found that the excitation spectra of Gd^{3+} ion-activated Ba_2YZrO_6 perovskite ceramic phosphor showed weak transition and inter-configurational 4 f^7-4 f^7 transitions of Gd^{3+} ions **(**Fig. 6**a)**. [83] And it exhibited the NB-UVB emission at 315 nm under 229 nm excitation **(**Fig. 6**b)**. They also used electron paramagnetic resonance (EPR) to characterize the resonance signal of Gd^{3+} ions in garnet compound $CaY_2Al_4SiO_{12}$ derived from cubic, octahedral or tetrahedral distortion sites. [84] Its emission spectra show $^6P_{5/2}\rightarrow{}^8S_{7/2}$ and $^6P_{7/2}\rightarrow{}^8S_{7/2}$ transitions with peaks at 308 nm and 314 nm.

By introducing a suitable sensitizer, the transfer of energy to Gd^{3+} can achieve efficient NB-UVB luminescence. Wang et al. reported energy transfer between Pr^{3+}, Pb^{2+}, or Bi^{3+} sensitizers and Gd^{3+}, achieving in more than 10 h NB-UVB afterglow, as illustrated in Fig. 6**c**. [124] Yu et al. designed a multilevel luminescence thermometer utilizing three excited ^6P_J ($J = 7/2,5/2,3/2$) crystal fields and spin-orbit split levels of UVB-emitting Gd^{3+} ions. [99] This was achieved by co-doping Pr^{3+} in $YAl_3(BO_3)_4$ and upconverting to its 4 $f^1$5d^1 configuration, which then efficiently transfers the energy to the ^6P_J energy level of Gd^{3+} (Fig. 6**d-e**)

Not only that, NB-UVB persistent luminescence can also be achieved with the assistance of trap levels. Under high energy ultraviolet or X-ray excitation, excited transition carriers are stored in trap levels. Upon cessation of excitation, the captured energy is continuously transferred

Table 1
Gd^{3+}-activated UV phosphors.

Groups	Materials	λ_{ex}(nm)	λ_{em}(nm)	E_g(eV)	Ref.
Phosphates	YPO_4	272	312	5.8[a]	[85]
	$LaPO_4$	272	312	4.65[a]	[86]
	YPO_4:Gd^{3+},Sb^{3+}	254	312	–	[87]
	$LaPO_4$: Gd^{3+},Bi^{3+}	275	312	–	[88]
	$LiSrPO_4$	275	312	4.45[a]	[89]
	$NaSrPO_4$	273	313	4.52[a]	[90]
	$Sr_2P_2O_7$	X-rays	312	5.11[a]	[9]
	$Sr_3P_4O_{13}$	272	312	5.21[a]	[91]
	$CaMgP_2O_7$	274	314	–	[92]
	$Ca_9Mg(PO_4)_6F_2$	274	313	–	[28]
Borates	$RbBaBP_2O_8$	273	312	4.22	[93]
	YBO_3:Bi^{3+},Gd^{3+}	273	313	5.17	[94]
	$Sr_2Mg(BO_3)_2$	276	313	4.39	[95]
	$Sr_2Mg(BO_3)_2$:Gd^{3+}, Pb^{2+}	254	330	4.39	[96]
	LaB_3O_6:Gd^{3+},Bi^{3+}	254	311	4.54	[97]
	$YBaB_9O_{16}$:Gd^{3+},Bi^{3+}	254	312	–	[98]
	$YAl_3(BO_3)_4$:Gd^{3+}, Pr^{3+}	450	310	5.16	[99]
	$LiSr_4(BO_3)_3$:Gd^{3+}, Pr^{3+}	276	313	4.19[a]	[100]
Aluminates	Al_2O_3	273	314	5.85	[101]
	$Ca_3Al_2O_6$	273	314	–	[102]
	$CaAl_2O_4$	273	314	4.47	[103]
	$SrAl_2O_4$	273	314	4.14	[104]
	$LaAl_{11}O_{18}$	273	314	–	[105]
	$LaMgAl_{11}O_{19}$	273	313	4.21[a]	[106, 107]
	$CaY_2Al_4SiO_{12}$	273	314	–	[84]
Silicates	Ba_2SiO_4	X-rays, 273	315	4.63	[108, 109]
	$Na_3YSi_2O_7$	273	313	4.01[a]	[110]
	$Ca_2MgSi_2O_7$	275	314	4.6	[111]
	$Sr_2MgSi_2O_7$	273	313	4.5	[112]
	$CaLa_4Si_3O_{13}$	228	314	4.48[a]	[113]
	$Ca_3MgSi_2O_8$	273	313	4.88	[114]
	Li_2MgSiO_4	272	314	4.94	[115]
	$Ca_2La_8(SiO_4)_6O_2$	230	314	4.48[a]	[116]
	Y_2SiO_5	257	316	4.77	[117]
Zirconates	$CaZr_4O_9$	274	313	3.84	[118]
	$Y_4Zr_3O_{12}$	274	313	4.11[a]	[119]
	ZrO_2	275	314	3.53	[120]
	Ba_2YZrO_6	229	315	–	[83]
Others	SrY_2O_4	275	315	3.7	[121]
	$Gd_3Ga_5O_{12}$	273	311	2.9	[122]
	$SrMgF_4$	274	313	6.69	[123]
	$BaMgF_4$	274	313	6.79	[123]

[a] DFT calculated bandgap value

from the Pr^{3+} 4f5d emission energy level to the Gd^{3+} ^6I_J or ^6P_J level, producing persistent emission at 311 nm. [98,108]

Excellent heat-resistance performance can also be obtained by doping Gd^{3+} into the highly rigid structure. Yang et al. doped Gd^{3+} in the highly rigid diamond-like structure $RbBaBP_2O_8$ to obtain a phosphor with NB-UVB emission. The fluorescence intensity was 93% of the initial value at 423 K, showing excellent heat-resistance performance, as shown in Fig. 6**f**. [93]

High-energy X-ray sources have also become attractive charging sources for Gd^{3+}, especially in wide bandgap host. For instance, an X-ray charged $LaMgAl_{11}O_{19}$:Gd^{3+} persistent phosphor was reported by Zhao et al. [106] Zhang et al. reported that $Sr_2P_2O_7$:Gd^{3+} phosphors showed NB-UVB persistent luminescence at 312 nm for more than 24 h. [9] The ultraviolet camera can clearly detect the afterglow signal uninterrupted by bright ambient light (Fig. 6**g-h**).

3.2. Pr^{3+}-activated phosphors

Due to its unique 4 $f^15d^1 \rightarrow 4$ f^2 interconfigurational energy transition mechanism, trivalent Pr^{3+} ion exhibits effective UVC emission in suitable crystal fields, which has attracted much attention. To date, dozens of Pr^{3+}-activated UV phosphors have been developed, and commonly used host include silicate (such as Y_2SiO_5), melilites (such as $Ca_2Al_2SiO_7$), fluorides (such as Cs_2NaYF_6), phosphates (such as $LaPO_4$), and garnets (such as $Lu_3Al_5O_{12}$), as summarized in Table 2.

As early as 2006, Sun et al. found broadband emission of Pr^{3+} doped Y_2SiO_5 at 270–350 nm. [138] In the lower density β-$Y_2Si_2O_7$:Pr^{3+}, the smaller degree of crystal field splitting causes a blue shift to 270 nm, but also shows a certain percentage of visible light emission (originating from the f-f internal configuration transition). [126] This variability in the stimulated emission is affected by the electronic structure of the matrix and the different positions of the crystal field-induced 4 f^15d^1 energy level splitting.

When the crystal field is too weak, the 4 f^15d^1 excited state of Pr^{3+} produces a smaller field splitting effect, and the spectral blue shift is not obvious or even redshift. When the crystal field is too strong, the excited state of Pr^{3+} 4 f^15d^1 produces a larger crystal field splitting effect, resulting in blue shift of Pr^{3+} 5d-4 f electron transition and over amplitude blue shift. In the past studies, researchers have conducted extensive spectral regulation studies on Eu^{2+} and Ce^{3+} ions emitted by typical d→f transitions, but no regular understanding has yet been formed on Pr^{3+}. Liang et al. reported a Pr^{3+}-doped garnet $Lu_3Al_{5-x}Ga_xO_{12}$ (x = 0, 2, 3) with tunable long afterglow in the UVB region. [137] By increasing the Ga substitution content, the modulation of the energy band structure led to a decrease in the bottom of CB from −1.68 eV to −2.49 eV. Meanwhile, the $5d^1$ configuration of Pr^{3+} (from −3.10 eV to −2.83 eV) is increased, realizing the luminescence spectra blue-shifted from 308 nm to 298 nm under excitation of 254 nm UV light (Fig. 7**a**). When Ga completely replaces Al, there is only visible light emission from the f-f transition. Further, Cr^{3+} ions were co-doped into the sample to enhance the UVB sustained luminescence performance of the $Lu_3Al_3Ga_2O_{12}$:Pr^{3+} phosphor. $Lu_3Al_3Ga_2O_{12}$:Pr^{3+},Cr showed PersL for more than 60 h by co-doping Cr and observed two obvious excitation band (Fig. 7**b-c**). Fig. 7**d** illustrated UVB photoluminescence and PersL images recorded at different time using an UV camera.

In addition to the excitation of UV, Pr^{3+} ion usually has absorption peaks in the 490–520 nm, 560–630 nm, 950–1100 nm, 1300–2200 nm region, stemming from $^3H_4$ ground state transitions to $^3P_{0,1,2}$, $^1I_6$, $^1D_2$, $^1G_4$ and $^3F_{2,3,4}$ state. High-energy X-rays can also effectively excite Pr^{3+} ion to achieve UV emission. Zhou et al. also report Li_2CaGeO_4:Pr^{3+} with multi-responsive UV emission properties (Fig. 7**e**). [130] Yang et al. showed the afterglow images of $Cs_2NaY_{0.99}F_6$:0.01Pr^{3+} phosphor irradiated by different excitation wavelengths of 793 nm, 730 nm and 450 nm (Fig. 7**f**). [134] Specifically, exposure to 450 nm of light produces stronger UVC afterglow than exposure to 730 nm and 793 nm of light. Pan et al. reported an excited UVC long afterglow of up to 10 hours in Pr^{3+}-doped $Ca_2Al_2SiO_7$ for labeling in bright environments. [5] The same phenomenon is also found in its isomorphic melilites $Sr_2MgSi_2O_7$. [136] Yan et al. reported that $LiLuSiO_4$:2%Pr^{3+} showed PL and persistent luminescence at 279 nm under 247 nm excitation (Fig. 7**g**). [129] By co-doping Sm^{3+} ions as electron trap, UVC afterglow intensity and time significantly enhance.

So far, the discovery of UV phosphors has been mainly dependent on experimental trial-and-error approaches. Li et al. proposed that topochemical reactions was shown to accelerate the discovery of emerging UV phosphors, especially long afterglow phosphors. [132] The thermodynamic charge transition energy levels of defect states are determined by first principles calculation, which helps to test whether the candidate structures are suitable as host for the afterglow. The Pr^{3+}-doped $LaPO_4$ was then found to have a UVC afterglow lasting longer than 2 hours through topochemical reactions.

3.3. Bi^{3+}-activated phosphors

Bi^{3+} ion is emerging as a favored UV luminescent center because of its unique emission characteristics. [20,139] In the study of Bi^{3+}-doped

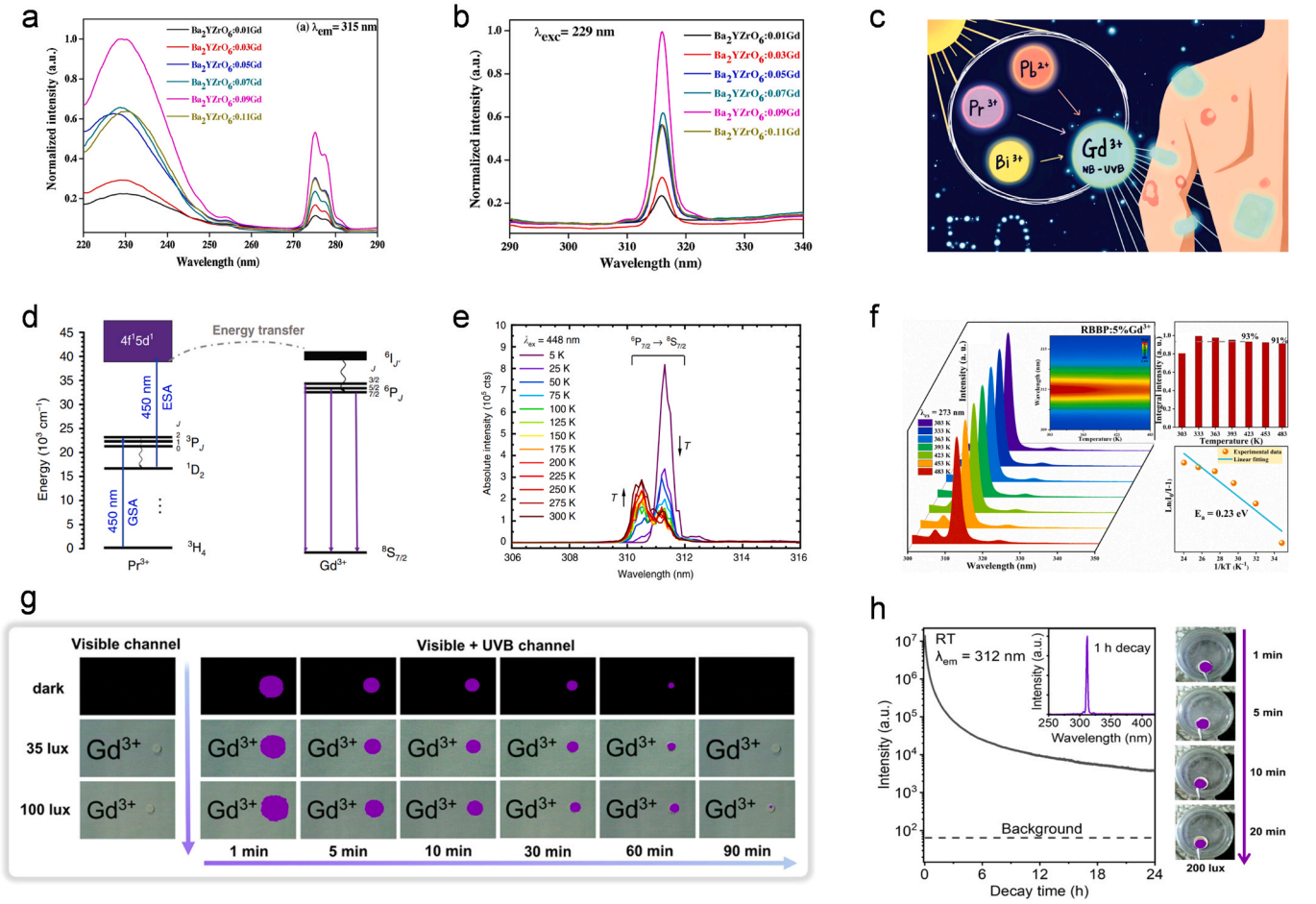

Fig. 6. **a**. PLE and **b**. PL spectra of Ba_2YZrO_6:xGd ($0.01 \leq x \leq 0.11$) phosphors [83]. Copyright 2020. **c.** Schematic diagram of Bi^{3+}, Pr^{3+} and Pb^{2+} ions energy transfer to Gd^{3+} [124]. Copyright 2021. **d**. Indirect upconversion excitation scheme of 4 f^15d^1 configuration of Pr^{3+} to Gd^{3+}. GSA and ESA represent the ground state absorption and the excited state, respectively [99]. Copyright 2021. **e**. High-resolution temperature dependence upconversion PL spectra of $YAl_3(BO_3)_4$:0.7%Pr^{3+}, 20%Gd^{3+}. **d**. NB-UVB persistent luminescence images and **e.** afterglow decay curves of the $Sr_2P_2O_7$:Gd^{3+} phosphor after irradiation by an X-ray beam [9]. Copyright 2022. **f**. Temperature-dependent normalized PL intensity of $RbBaBP_2O_8$:5%Gd^{3+} from 303 to 483 K [93]. Copyright 2022.

Table 2
Pr^{3+}-activated UV phosphors.

Groups	Materials	λ_{ex}(nm)	λ_{em}(nm)	E_g(eV)	Ref.
Silicates, germanates	Y_2SiO_5	252,450,488	260–345, 460–660	3.78	[125]
	β-$Y_2Si_2O_7$	248,450,488	250–345, 460–660	3.67	[126]
	Lu_2SiO_5	250	260–350	4.56	[127]
	Ba_2SiO_4	450	265		[108]
	Li_2SrSiO_4	450	250–340	4.65	[128]
	$LiLuSiO_4$	247	279		[129]
	Li_2CaGeO_4	X-rays, 240, 450, 980	250–320	3.80	[130]
	$BaLu_2Al_2Ga_2SiO_{12}$	254	301	4.85	[131]
Phosphates	La/YPO_4	X-rays	240	6.86	[132,133]
Fluorides	Cs_2NaYF_6	X-rays, 793, 730, 450	200–320	6.86[a]	[134]
	$LiYF_4$	488	260–360	7.84	[25]
Melilites	$Ca_2Al_2SiO_7$	233	268	4.32	[5]
	$Ca_{1.5}Sr_{0.5}Al_2SiO_7$	241	270	4.2	[135]
	$Sr_2MgSi_2O_7$	232	243	4.53[a]	[136]
Garnets	$(Ca_{1.5}Y_{1.5})(Al_{3.5}Si_{1.5})O_{12}$	245	266, 311	–	[12]
	$Y_2GdAl_2Ga_3O_{12}$	283	311	–	[124]
	$Lu_3Al_2Ga_3O_{12}$	278	298	–	[137]
	$Lu_3Al_3Ga_2O_{12}$	279	302	–	[137]
	$Lu_3Al_5O_{12}$	285	308	4.94	[137]

[a] DFT calculated bandgap value

UV-emitting phosphors, phosphates, borates, germanates, and garnets have been investigated as host materials for intense tunable UV emission (Table 3).

Notably, the tunable UV emission of Bi^{3+} ion tailors by modulating the crystal field. Selective occupation of Bi^{3+} ion in $Sr_3Sc_2Ge_3O_{12}$ with distinct luminescence properties was reported by Miao et al., as depicted

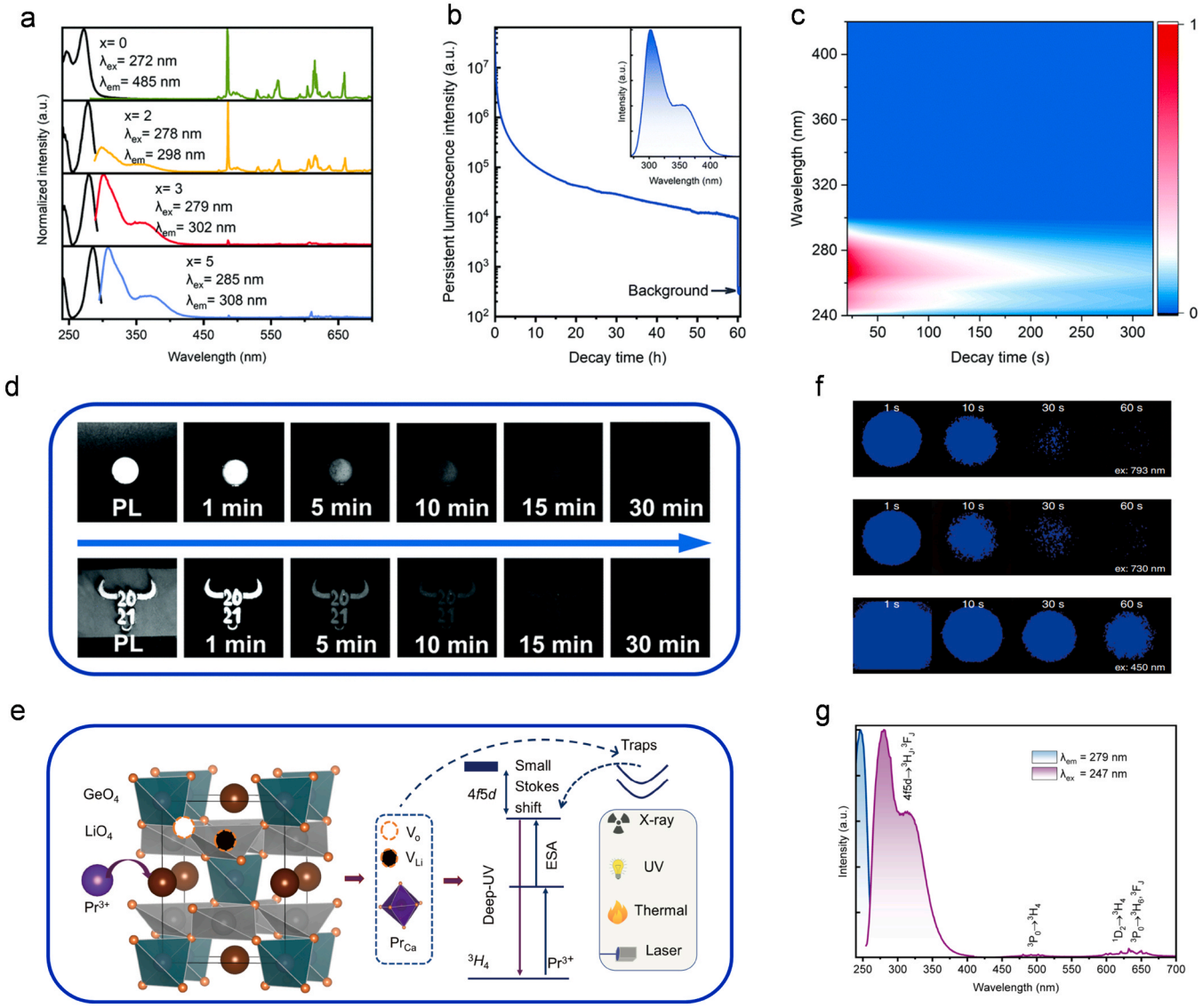

Fig. 7. **a**. PLE and PL spectra of $Lu_3Al_xGa_{5-x}O_{12}:Pr^{3+}$ ($x = 0$, 2, 3, and 5) phosphors. **b**. Decay curve of $Lu_3Al_3Ga_2O_{12}:Pr^{3+}$,Cr phosphor. **c**. 2D PerL excitation profile spectrum of the $Lu_3Al_3Ga_2O_{12}:Pr^{3+}$,Cr phosphor. **d.** PerL images [137]. Copyright 2021. **e**. Schematic illustration of $Li_2CaGeO_4:Pr^{3+}$ with multi-responsive UV emission [130]. Copyright 2021. **f**. UVC images of $Cs_2NaY_{0.99}F_6$:0.01Pr^{3+} phosphors under different wavelength laser irradiation with 793 nm, 730 nm, and 450 nm [134]. Copyright 2018. **g**. PLE and PL spectra of the $LiLuSiO_4$:2%Pr^{3+} phosphor [129]. Copyright 2022.

in Fig. 8**a**. [147] Bi^{3+} occupying the Sr^{2+} site produces strong cyan photoluminescence (386 nm excitation). Bi^{3+} at the Sc^{3+} site produces UVA photoluminescence (289 nm excitation) and persistent luminescence. Li et al. also created a wide band gap (5.88 eV) $BaSc_2Ge_3O_{10}$ lattice environment for Bi^{3+}, and realized the UV emission centered at 370 nm **(**Fig. 8**b).** [145] The IQE and EQE at room temperature reached 81.0% and 49.32%, respectively.

Lyu and co-workers reported a systematic study of the spectral modulation scheme of Bi^{3+} doped ARE(Si,Ge)O_4 (A=Li, Na; RE=Y, Lu) system using vacuum-referenced binding energy (VRBE) -assisted energy-band engineering (Fig. 8**c**). [160] In this way, in the garnet-structured ARE(Si,Ge)O_4, the A-site cation has an important modulating effect on the crystal field strength in which the Bi ion is located. In contrast, the RE position and the Si/Ge positions have only a weak effect.

Recently, persistent phosphors doped with Bi^{3+} ion have been extensively studied in terms of UV emission. Bi^{3+} ion can produce PersL in different host materials by modulating the CB/VB through energy band engineering, as well as controlling the capture and de-capture processes through defect modulation.

Liu et al. modulated PersL emission spectra based on energy band engineering. [162] The band gap of $LuXO_4:Bi^{3+}$ (X = V, Nb, Ta, and P) was adjusted from ~4 eV to 9 eV using B-site cation substitution, which tailored the persistent luminescence from 550 nm to 230 nm (Fig. 8**d-e**). Shi et al. found that $LiYGeO_4:Bi^{3+}$ displays PL with a peak at 365 nm, achieving a super-long UVA persistent luminescence of more than 300 hours (Fig. 8**f**). [157] And it is ascribed to the absence of Li creating point defects. It is worth noting that Shao et al. also reported the UVA mechanoluminescence property of this Bi^{3+} doped $LiYGeO_4$ material for the first time. [139] A local piezoelectric field is produced under the stimulation of mechanical force, and the carriers trapped in the point defect directly migrate to the excited state of Bi^{3+} through the tunneling effect, and mechanoluminescence is finally observed. A multimodal anti-counterfeiting strategy was proposed in $Ca_3Al_2Ge_3O_{12}:Bi^{3+}/Ln^{3+}$ (Ln = Tb, Eu, Sm, and Dy) by Zhang et al. [155] It's the energy transfer from Bi^{3+} to Ln^{3+} that UVB persistent luminescence is more than 20 hours, as shown in Fig. 8**g**.

With these advances, we can find that the emission of Bi^{3+} ion has

Table 3
Bi^{3+}-activated UV phosphors.

Groups	Materials	Excitation wavelength (nm)	Emission wavelength (nm)	Band gap (eV)	Ref.
Ortho-phosphates	YPO_4	X-rays	240	5.81	[140]
	$LaPO_4$	X-rays	231	5.81	[55]
	$LuPO_4$	166	248	8.97	[141]
	$Ca_9Y(PO_4)_7$	197	250, 275	–	[142]
Borates	$GaBO_3$	276	290	3.86	[143]
	$ScBO_3$	284	300	4.12	[143]
	$InBO_3$	285	400	2.66	[143]
	$LuBO_3$	287	305	5.30	[143]
Germanates	$Mg_2Lu_2Ge_3O_{11}$	254	310	6.00	[144]
	$BaSc_2Ge_3O_{10}$	305	370	5.88	[145]
	$Mg_4Y_{1.2}Lu_{0.8}Ge_3O_{13}$	283	325	–	[146]
	$Sr_3Sc_2Ge_3O_{12}$	289	333	3.79	[147]
	$Mg_8Lu_2Ge_6O_{23}$	285	311	–	[148]
	Mg_2GeO_4	310	350		[149]
Garnets	$(Y,Gd)_3Ga_5O_{12}$	289	313	–	[150]
	$Y_2GdAl_2Ga_3O_{12}$	254	311	–	[124]
	$Y_3Ga_5O_{12}$	291	313	6.58	[151]
	$Y_3Al_5O_{12}$	275	302	3.67	[151]
	$Lu_3Al_5O_{12}$	272	298	4.94	[151]
	$Lu_3Ga_5O_{12}$	254	313	6.55	[152]
	$Y_3Ga_5O_{12}$	Sunlight	313	3.35	[153]
	$Ca_3Ga_2Ge_3O_{12}$	245, 285	317	4.04	[154]
	$Ca_3Al_2Ge_3O_{12}$	265	313	3.50[a]	[155]
	$Gd_3Ga_5O_{12}$	290	316	6.49	[156]
	$LiYGeO_4$	254	365	3.82[a]	[157]
	$LiYGeO_4$	X-ray	352	3.82[a]	[158]
	$LiScGeO_4$	297	361	3.80	[159]
	$Na_{1-x}Li_xLuGeO_4(x=0–1)$	308	393–350	–	[160]
	$LiLuSiO_4$	207	356	–	[160]
	$LiLuGeO_4$	230	360	–	[160]
	$LiYSiO_4$	207	363	–	[160]
	$NaGdGeO_4$	310	400	4.87	[161]
Others	$LuVO_4$	X-rays	455	4.86	[162]
	$LuNbO_4$	X-rays	236	5.27	[162]
	$LuTaO_4$	X-rays	389	6.18	[162]
	$CaSb_2O_6$	297	290	4.53	[163]
	$SrSb_2O_6$	301	319	4.28	[163]
	$CdSiO_3$	233	360	2.57	[164]
	$GdAlO_3$	290	333	3.24	[165]
	$SrLaAlO_4$	X-rays	380	2.90[a]	[166]

[a] DFT calculated bandgap value

wide tunability in the visible-UV region. Among the Bi^{3+} activated phosphors, only phosphates with wide band gap provide a suitable crystal field strength for the UVC emission of Bi^{3+}. The mixed density functional method calculates the thermodynamic charge transfer levels ε(+3/+4) and ε(+2/+3) and the $^3P_1 \rightarrow {}^1S_0$ transition excited level induced by Bi^{3+} in the YPO_4. [22] The trap depths of ε(+3/+4) and ε(+2/+3) are 1.04 eV above VBM and 2.31 eV below CBM in YPO_4, respectively. While the excitation level of $^3P_1 \rightarrow {}^1S_0$ band transition (i.e., $^3P_1$) is more than 2 eV below CBM. Liu and co-workers reported YPO_4:Bi^{3+} with more than 2 h UVC afterglow centered at 240 nm, ascribed to transition of Bi^{3+} ion. [140]

3.4. Other ion-activated phosphors

Pb^{2+} doped phosphors, including silicates, phosphates and sulfates, have been extensively studied for decades. The emission band of Pb^{2+} ion can be regulated from the visible to UV region, and are largely dependent on the symmetry of substitution site, ligand ions, and host matrix. [167]

Silicates are good candidates for Pb^{2+} ion since they are inexpensive and readily available. $BaSi_2O_5$:Pb^{2+} as a UV-emitting phosphor was firstly used for photocopying. [168] Wang et al. developed a Pb^{2+}-activated UVB persistent phosphor $Sr_3Y_2Si_6O_{18}$:Pb^{2+}, displaying a broadband emission at 299 nm for more than 12 h (attributed to the Pb^{2+} $^3P_1 \rightarrow {}^1S_0$ transition) (Fig. 9**a**). [124] Since the $^3P_1$ luminescence energy level of Pb^{2+} overlaps with the ^6P_J level of Gd^{3+}, there is an energy transfer from Pb^{2+} to Gd^{3+} when the Y^{3+} ions are replaced by Gd^{3+} ions. The resulting $Sr_3Gd_2Si_6O_{18}$:Pb^{2+} material shows NB-UVB persistent luminescence for up to 12 hours.

By adjusting the cation ratio (Sr/Ba) in Pb^{2+} doped $Sr_2MgSi_2O_7$, Wang et al. redshifted the emission spectral from 333 nm to 383 nm (Fig. 9**b-c**). [169] Liang et al. completely replaced Si with Ge to obtain the isomorphic compound $Sr_2MgGe_2O_7$, which has an UV emission of Pb^{2+} and a peak value of 370 nm. [172]

Inorganic borates have the advantage of low synthesis temperature, high physicochemical stability and high UV transmittance. Due to energy transfer, Pb^{2+} doped $Li_6Gd(BO_3)_3$ also shows NB-UVB emission with peak emission located at 313 nm. [173] Esra Yıldız et al. studied the concentration quenching of Pb^{2+} ions in SrB_4O_7:Pb^{2+} and concluded that it mainly originates from the migration of excitation energy to the quenching centers. [174]

Ce^{3+} ions are common yellow emission activators, but they also exhibit UV emission in suitable crystal fields. Under 225 nm excitation, the central luminous wavelength of Ce^{3+} doped $Ca_9Y(PO_4)_7$ phosphor is at 346 nm due to the transition from $5d^1$ to $4\,f^1$. [142] The PLE spectrum shows multiple bands from 180 ~ 350 nm, attributed to the crystal field splitting in the Ce^{3+} 5d state, as shown in Fig. 9**d**. In 2019, Xie et al. further investigated the occupation of Ce^{3+} ions in the $Ca_9La(PO_4)_7$ lattice [175]. It was found that Ce(1) emission was associated with the 8-coordinated Ca site, and Ce(2) emission was associated with the 6-coordinated La site by spectroscopic and luminescence kinetic studies. Shirmane et al. found strong UV emission in conventional yellow-green emitting YAG:Ce nanocrystals, which shows a fast decay time of about 7 ns and a high intensity resolved excitation band with a peak of 5.9 eV.

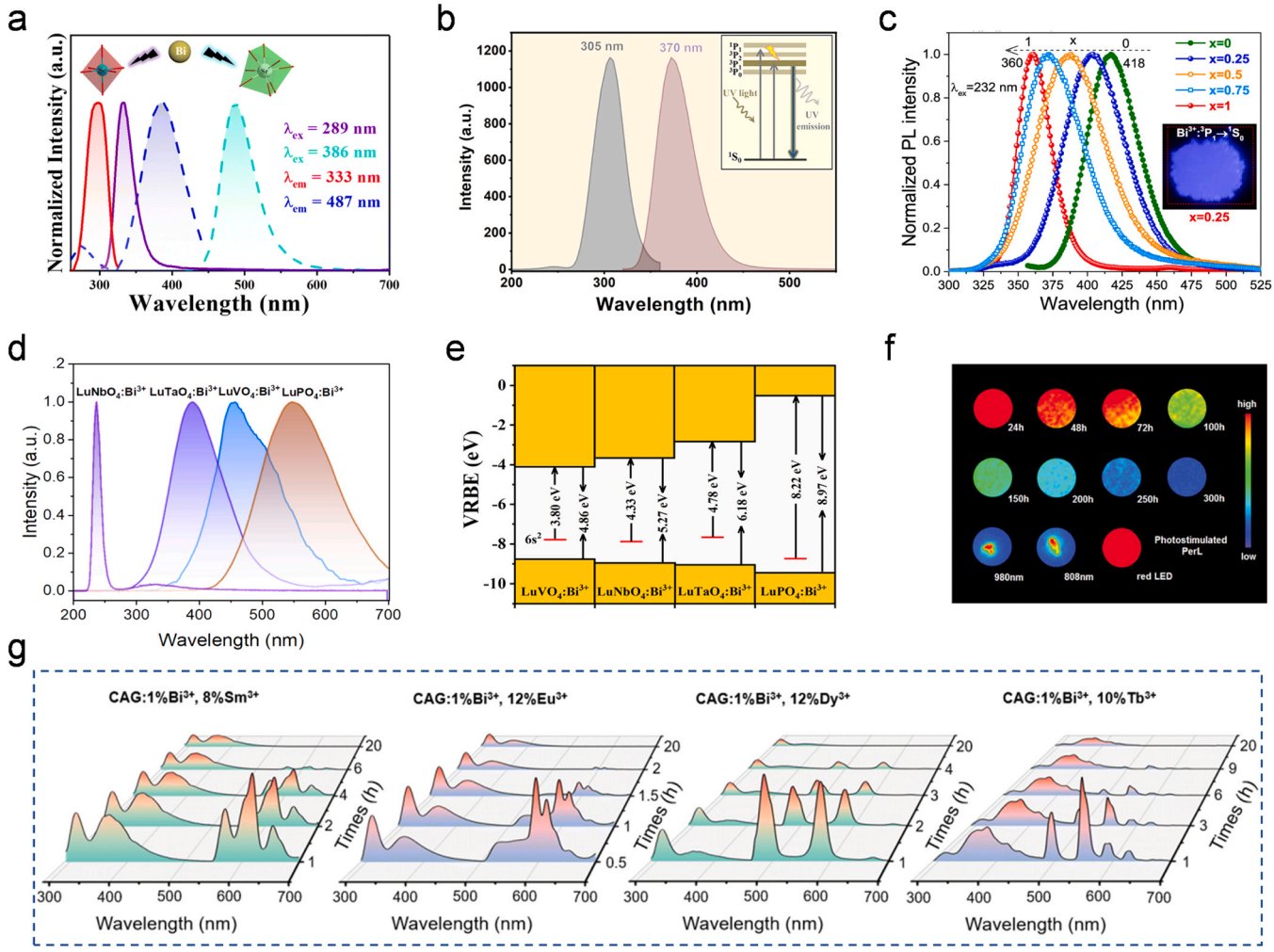

Fig. 8. a. PLE and PL spectra with selective occupation of Bi^{3+} ion in $Sr_3Sc_2Ge_3O_{12}$. [147] b. PLE and PL spectra of $BaSc_2Ge_3O_{10}$:0.005Bi^{3+} [145]. Copyright 2023. c. PL spectra of $Na_{1-x}Li_xLuGeO_4$: 0.01Bi^{3+} and insert afterglow photograph [160]. Copyright 2020. d. Persistent luminescence spectra after excitation of X-rays and e scheme of VRBE for $LuXO_4$:Bi^{3+} (X=V, Nb, Ta, and P) [162]. Copyright 2022. f. UVA PerL images of $LiYGeO_4$:Bi^{3+} [157]. Copyright 2019. g. Afterglow emission spectra of $Ca_3Al_2Ge_3O_{12}$:1.0% Bi^{3+}/*x*% Ln^{3+} [155]. Copyright 2023.

[176]

UVA persistent luminescence of CaB_2O_4:Ce^{3+} phosphor is more than 15 h. [170] Lifetime measurements indicate that the 5d→4 f transition of Ce^{3+} cause the emission centered at 365 nm (Fig. 9**e**). The lowest energy level of Ce^{3+} $5d^1$ is below the CB ~ 0.97 eV, and the persistent luminescence results from radiative transition between Ce^{3+} 5d→2 $f_{5/2, 7/2}$ energy levels. Wang et al. found that Ce-doped $NaLuF_4$ shows a strong broad emission centered at 298 nm under X-ray irradiation (Fig. 9**f**). [171]

aDFT calculated bandgap value

4. UV carbon dot-based nanomaterials

CDs is a new kind of non-metal luminescent nanomaterial with the advantages of high efficiency, adjustable luminescence, good photostability, biocompatibility, and environmental protection. To date, CDs have shown colorful emission from the deep blue to the NIR, yet obtaining CDs with UV emission remains a great challenge, which needs to carefully design the structure of CDs and overcome the quenching caused by aggregation.

In 2012, Lau et al. prepared UV-emitting GQDs for the first time using microwave-assisted hydrothermal (MAH) (Fig. 10**a**). [4] Its UVB emission wavelength is 303 nm under 197 nm laser excited, and the PLQY is 7–11% (Fig. 10**b**). It is worth noting that the size of GQDs has no effect on the emission wavelength. The results show that the unique optical properties are mainly due to the self-passivated layer on the surface of GQDs. When coated on blue LED, GQDs are capable of converting blue light to white light, showing significant promise for applications in the field of UV photonic devices.

In 2016, Anappara et al. synthesized UV luminescent CDs using tannic acid by MAH method. [192] The luminescence of water-soluble CDs at 370 nm does not vary with the excitation wavelength (Fig. 10**c**). Moreover, the CDs can sensitively detect picric acid in water-based media with a detection limit of 0.6 pM.

In 2019, Shan et al. reported UV emitting CNDs with emission located between 280 and 300 nm (Fig. 10**d**). [41] The CN solution was obtained by chromatography. The emission peak of CNDs is located at 290 nm, and two shoulders were also observed at 282 and 300 nm in ethanol solution (Fig. 10**e**). The PLQY of CNDs at 250 nm excitation was 31.6%, arising from the radiative recombination of nuclear (π-π*) carriers and surface passivation (Fig. 10**f**). LEDs with strong UV emission were prepared using CNDs as phosphors.

However, similar to the above studies, solvents or polymeric substrates are demanded to stabilize the emission centers in most CDs. Solid-state luminescent materials can be directly and conveniently used in photonic devices in contrast to materials that only exhibit efficient luminescence in specific media. [193] Additionally, CDs with ultra-narrow half-height widths (FWHM), which have potential

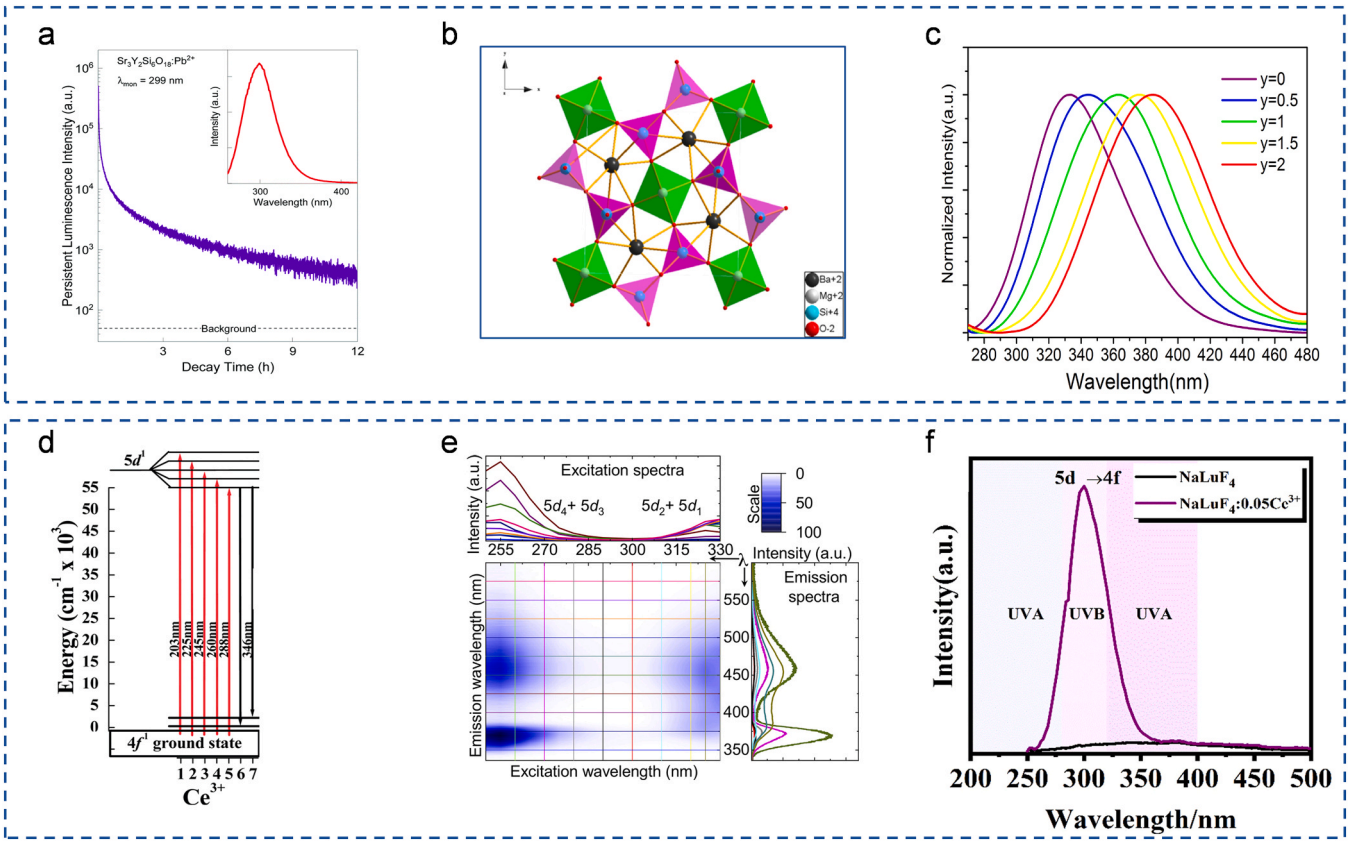

Fig. 9. a. PerL decay curves of $Sr_3Y_2Si_6O_{18}:Pb^{2+}$ phosphor [124]. Copyright 2021. **b.** Crystal structure of $Sr_2MgSi_2O_7$. **c.** PL spectra of $Sr_{2-y}Ba_yMgSi_2O_7:0.02Pb^{2+}$ (y=0–2, λ_{ex} = 258 nm) [169]. Copyright 2020. **d.** Energy level scheme of $Ca_9Y(PO_4)_7:Ce^{3+}$ phosphors [142]. Copyright 2011. **e.** PL contour plots for CaB_2O_4:0.1% Ce^{3+} phosphor [170]. Copyright 2019. **f.** X-ray excited luminescence spectra of Ce^{3+} doped $NaLuF_4$ [171]. Copyright 2021.

Table 4
Pb^{2+} or Ce^{3+}-activated UV phosphors.

Activators	Materials	λ_{ex}(nm)	λ_{em}(nm)	E_g(eV)	Ref.
Pb^{2+}	$Ba_2MgSi_2O_7$	258	383	4.45	[169]
	$Sr_2MgSi_2O_7$	258	333	4.50	[169]
	$Sr_2MgGe_2O_7$	280	370	3.60	[172]
	$Sr_3Y_2Si_6O_{18}$	254	299	–	[124]
	$Sr_3Gd_2Si_6O_{18}$	254	311	–	[124]
	$CaTiO_3$	345	365	2.31	[167]
	$CaSO_4$	200	235	5.95	[177]
	$SrSO_4$	220	285, 380	5.92	[177]
	$BaSO_4$	220	340	5.95	[177]
	$NaSr_4(BO_3)_3$	289	370	3.98	[178]
	$Sr_2Mg(BO_3)_2:Pb^{2+}$	254	330	4.39	[96]
	$Ba_2Mg(BO_3)_2$	293	381	4.47	[179]
	SrB_2O_4	270	363	4.95	[180]
	$Li_6Gd(BO_3)_3$	242	313	2.74	[173]
	SrB_4O_7	239	300	7.12	[174]
	$Li_6CaB_3O_{8.5}$	268	307	–	[181]
	$Ba_2Be_2B_2O_7$	284	396	–	[182]
	$KCa_4(BO_3)_3$	260	335	4.59	[183]
Ce^{3+}	ZnO	270	380	3.27	[184]
	$Ca_9Y(PO_4)_7$	318	396	–	[185]
	$CaAl_4O_7$	273	330, 360	4.00	[186]
	$CaAl_2O_4$	300	370	4.47	[186]
	$CaAl_{12}O_{19}$	262	329	4.35	[187]
	$LaBaB_9O_{16}$	274	335	–	[188]
	$LaBO_3$	270	355, 380	4.50	[189]
	$SrBPO_5$	315	365	4.01	[190]
	CaB_2O_4	337	365	7.77	[170]
	$NaLuF_4$	X-ray	298	–	[171]
	$Li_4SrCa(SiO_4)_2$	288	345	4.86	[191]

applications in high-efficiency LED devices [194] and high-resolution biomarkers [195], is also one of the research difficulties of solid-state CDs. [38]

Bi et al. adopted an sp^3 compartmentalization strategy to facilitate the binding of sp^3 bonds during hydrothermal synthesis of CDs utilizing glacial acetic acid (Fig. 11**a**). [48] In this way, the size of sp^2 conjugating units is significantly reduced and the PL emission moves to 308 nm in CDs (Fig. 11**b-c**). It also shows high PLQY (20.2%, λex = 265 nm) with narrow FWHM. More importantly, the luminescence properties of the UVB-CDs have high environmental robustness (Fig. 11**d-e**). This is attributed to the fact that the sp^2 domain is well delineated spatially by the sp^3 structural domain and the quenching effect caused by aggregation is minimized. This provides a reasonable approach for the preparation of solid UVB-CDs phosphors with wide application.

Unlike UV fluorescence, the key to inducing UV phosphorescence is the restriction on conjugation size and in-situ spatial of CNDs. [196] Shan et al. constructed UV phosphorescent CND using melamine as luminophore (Fig. 12**a**). [44] The phosphorescence peak at 348 nm was generated by modulating the size of the CND to 3.6 nm with a lifetime of 15.8 ms. The PLQY was about 31.7%, while the phosphorescence QY was about 16.2% (Fig. 12**b**). It is the orbital angular momentum of N atoms from p_x to sp^2 that provides the driving force for the population of triplet excitons. NaCNO crystals provide a rigid environment for CNDs and reduce the energy dissipation.

5. UV perovskite nanocrystals

Fig. 13 summarizes the PLQY corresponding to the different emission wavelengths of the state-of-the-art UV perovskite nanocrystals. Obviously, the UV emission of perovskite materials is mainly concentrated in the UVA band with longer wavelength. This is associated with the local

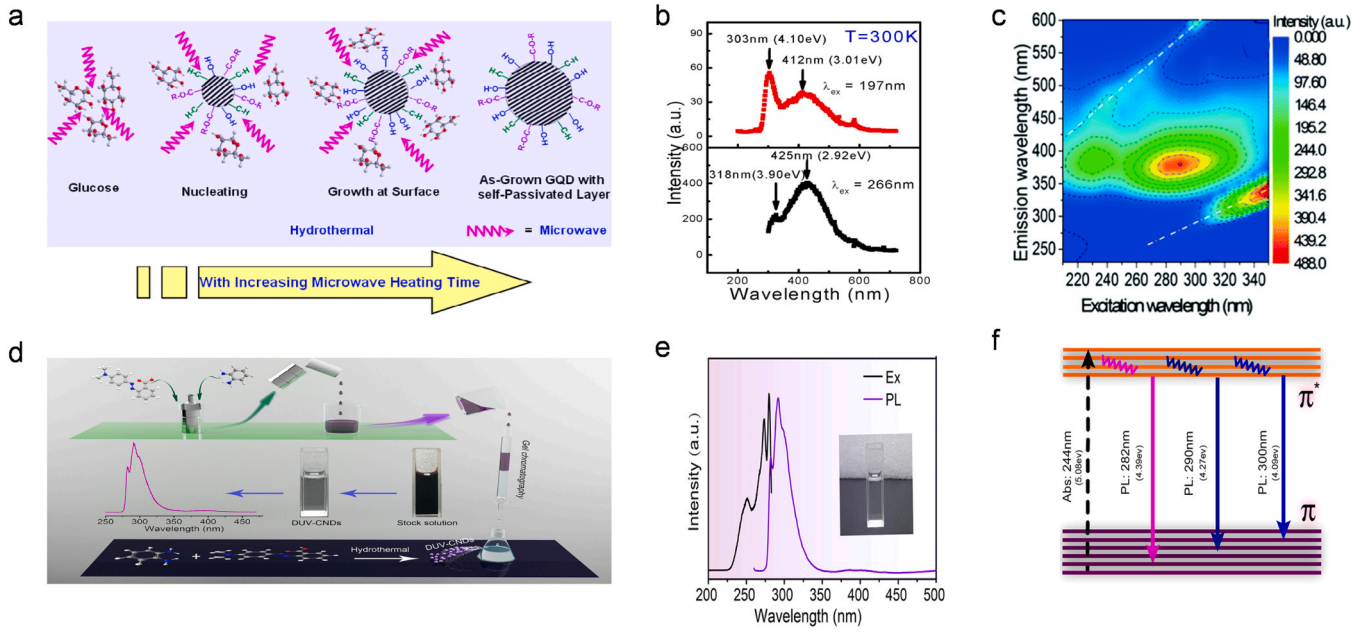

Fig. 10. **a.** MAH method preparation and **b.** PL spectra of GQDs [4]. Copyright 2012. **c.** PL Contour plot of CDs in water solution.[192] Copyright 2016. **d.** Schematic diagram of the preparation processes of the CNDs [41]. Copyright 2019. **e.** PLE and PL spectra of CNDs in ethanol solution [41]. Copyright 2019. **f.** Radiative recombination transition in CNDs [41]. Copyright 2019.

structure of perovskite itself and the large Stokes shift induced by UV excitation.

5.1. Lead halide perovskite

5.1.1. $CsPbX_3$ (X=Cl, Br)

Lead halide perovskite $CsPbX_3$ (X=Cl and Br) with color tunable emission shows great potential for lighting and display applications. [197] The crystal structure of $CsPbX_3$ is similar to that of oxide perovskite, with $[BX_6]^{4-}$ octahedral three-dimensional interconnects and a 12-coordination Cs^+ ion in a large cavity, as illustrated in Fig. 14**a**. [198] $CsPbX_3$ nanocrystals display narrow emission stemming from near-bandgap exciton recombination. [199] Their optical properties can be tailored by changing their size, shape, and halide composition. However, only $CsPbCl_3$ shows intrinsic UV emission, which is about 390 nm, and PLQY is only 1%. [200]

Moreover, $CsPbCl_3$ with different nano sizes, from three-dimensional nano-cubes, two-dimensional nanoplates, to one-dimensional nanorods, also showed the blue shift of PL. Compared with $CsPbCl_3$ nano-cubes (emission about 410 nm), the 1D $CsPbCl_3$ nanorod emission peak is blue-shifted to 385 nm (Fig. 14**b**). [201] Recently, Zhang et al. successfully tuned the thickness from 2.8 nm to 3.6 nm by reducing the solvothermal reaction time only, and achieved a blue shift to 391 nm in $CsPbCl_3$ nanoplates. [203]

Shen et al. introduced ammonium hexafluorophosphate while stripping the outermost surface of $CsPbX_3$ NC and passivating the defects. [202] The PLQYs of $CsPbCl_3$ increased to 25% at 398 nm. This simple post-treatment strategy has also been shown to be effective in enhancing the PLQYs of various $CsPbX_3$ nanocrystals in the entire visible wavelength range (Fig. 14**c**).

$CsPbCl_3$ can serve as a good accommodation for doping ions. These ions alter the pristine PL properties of perovskites by tailoring its intrinsic luminescence or introducing other emission band. Chen et al. reported high efficiency UV emission in $CsPbCl_3$ nanocrystals by incorporating cadmium ions, with an emission peak at 381 nm (Fig. 14**d**). [82] First principles calculations confirmed that blue shift emission originated from bandgap broadening. Subsequently, by using the surface passivation strategy of $CdCl_2$, UV PLQY of 60.5% was achieved, which is the highest value reported in perovskite so far. The PL decay kinetics of nanocrystals accelerates with increasing Cd^{2+} doping (Fig. 14**e**). The fast/slow decay compositions are attributed to the electrons trapped on the surface of nanocrystals and the exciton recombination in the internal structure, respectively.

5.1.2. Cs_4PbX_6 (X=Cl, Br)

0D inorganic perovskite-like Cs_4PbX_6 system shows interesting photoelectric properties owing to its strong localized exciton and high exciton binding energy (150–380 meV). [204,205] It appears as an optimal host-guest system where the PbX_6 octahedron is decoupled by the surrounding Cs ions in the wide band gap matrix, as shown in Fig. 15**a**. It's the complete isolation of the PbX_6 octahedron that results in strong quantum confinement and exciton-phonon interactions, forming exciton localization, self-capture, and polaron. Its special structure provides a good host for UV emissions. The radiative decay of the Frenkel exciton at the Pb^{2+} site is thought to be the source of the UV emission.

Nikl et al. firstly reported that the UV emission band of Cs_4PbCl_6 crystal at 355 nm belongs to the Pb^{2+} cationic excitons, which originated from the optical transition of $^3P_{0,1}\rightarrow{}^1S_0$ in the isolated $[PbCl_6]^{4-}$ octahedron. [207] Chen's group reported the presence of UV luminescence derived from Pb^{2+} in Cs_4PbCl_6 with a peak position of 358 nm. (Fig. 15**b**) [206] Doping of Mn^{2+} ions introduced a $^4T_{1\,g}\rightarrow{}^6A_{1\,g}$ transition from Mn^{2+} forbidden rotation at 600 nm. As increase the concentration of Mn^{2+}, the luminescence intensity of Mn^{2+} gradually increased, while that of UV gradually decreased, indicating that the energy of Pb^{2+} was effectively transferred to Mn^{2+}. This is further demonstrated by the reduced PL lifetime of Pb^{2+} (Fig. 15**c**). The same phenomenon was observed in $CsPbCl_3$. Interestingly, Xu et al. obtained the mixed phase of $CsPbCl_3$ and Cs_4PbCl_6 in Mn^{2+} doped cesium-lead chloride, appearing the near-band-gap exciton UV emission of Cs_4PbCl_6, whose emission is dependent on the excitation wavelength. [199]

And Yin et al. reported two broad UV emission signatures of Cs_4PbBr_6 at 340 nm and 400 nm, attributed to $^3P_1\rightarrow{}^1S_0$ and a D-state transition of Pb^{2+} ions, respectively. [56] D-state emissio is produced by the strong interaction between Pb^{2+} ions occupying Cs^+ sites and

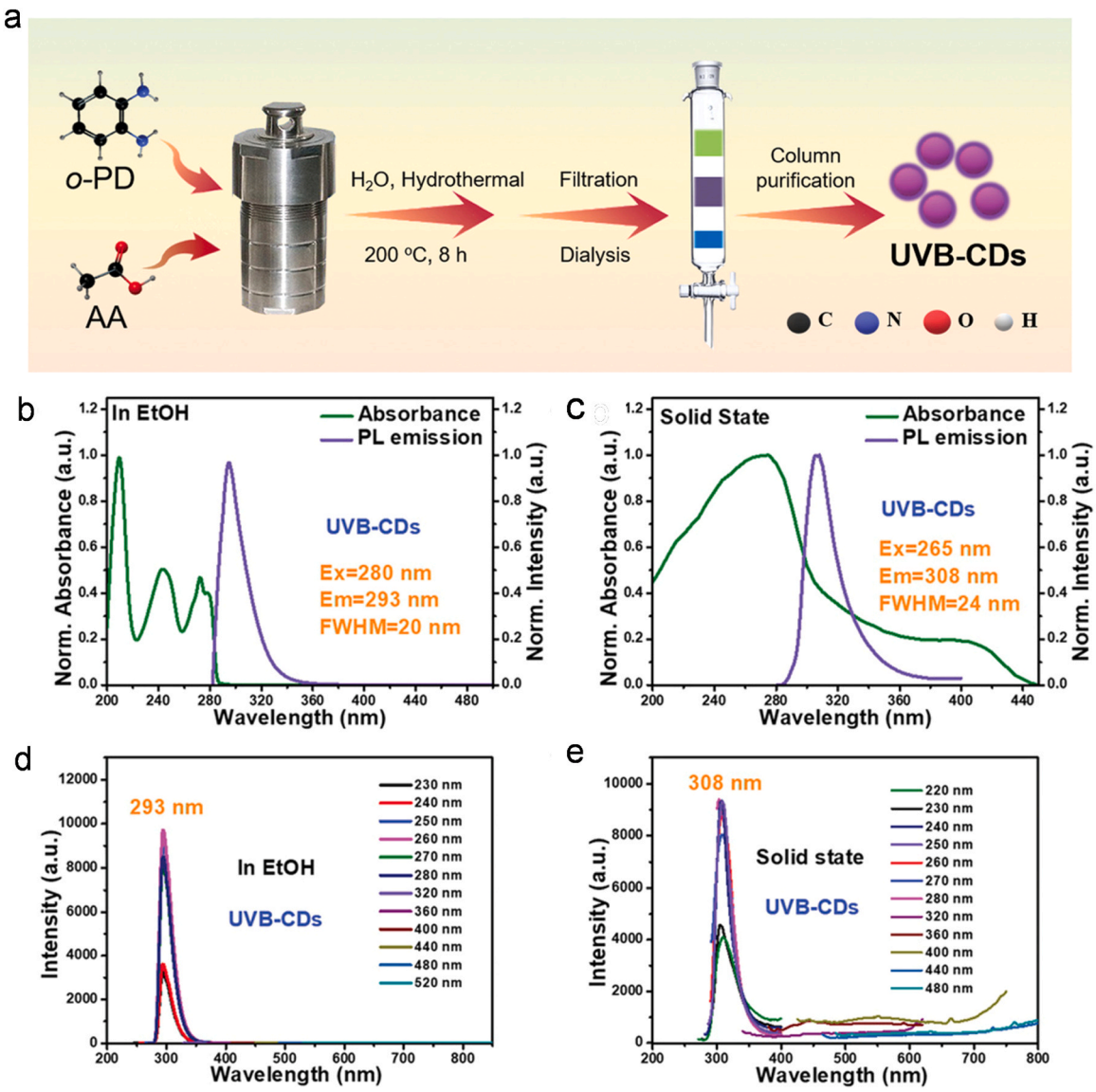

Fig. 11. a. Illustration of the synthesis process of the CDs. Absorption and PL spectra of **b**. UVB-CDs in EtOH solution; **c.** Solid state UVB-CDs. PL spectra of **d.** UVB-CDs in EtOH solution and **e.** UVB-CDs powder [48]. Copyright 2022.

$[PbBr_6]^{4-}$ octahedra. Arunkumar et al. showed that the phase stabilization of Cs_4PbX_6 can be enhanced by the addition of manganese to enhance the octahedral distortion and thus reduce the symmetry of PbX_6. [204] However, as the Mn concentration increases, the emission of Mn^{2+} from $Cs_4Pb(Br/Cl)_6$ increases and the UV emission (peak at 372 nm) quantum efficiency decreases from 6% to 5% (Fig. 15**d**). It suggests that Mn^{2+} plays a role in isolating the PbX_6 octahedra (Fig. 15**e**). Fig. 15**f** depicts the energy transfer among $^3P_{0,1} \rightarrow {}^1S_0$ transition, D-state emission of Pb^{2+} and Mn^{2+} in $Cs_4Pb(Br/Cl)_6$ perovskite.

5.2. Lead-free perovskite

Although lead halide perovskites exhibit excellent photoluminescence properties, the potential toxicity of lead and its rapid chemical decomposition at atmospheric humidity seriously hinder its commercialization. The exploration and development of stable and efficient lead-free perovskite has become a frontier research hotspot in the field of perovskite. [208]

Liu et al. found that $Cs_4CuIn_2Cl_{12}$ layered double perovskite rich in water molecules shows the increasement of PLQY from 0.12% to 1.70% at the UV band (320 ~ 400 nm) and induced a morphological transition (Fig. 16**a**). The mechanism is to convert the observed dark transition of self-trapped exciton relaxation into a radiative transition. Additionally, lead-free perovskite Cs_2HfCl_6 nanocrystals have attracted extensive attention because of their stability and environmental protection. [209] The crystal structure shows a typical cubic space group Fm-3m, where the tetravalent metal ion Hf occupies the central position, producing isolated $[HfCl_6]^{2-}$octahedra (Fig. 16**b**). [210] And Han et al. reported 378 nm UV emission from $[HfCl_6]^{2-}$ octahedral intrinsic emission in Cs_2HfCl_6 nanocrystals, and there is an increase of the emission intensity after decreasing excitation wavelength. [63]

Tang et al. have synthesized the 2D perovskite $Cs_3Bi_2X_9$ with ethanol as the main solvent using a simple green method. [213] It has a monoclinic hexagonal structure, in which each Bi atom forming an octahedron with the nearest six X (X: Cl, Br, I) atoms and an X-Bi-X angle of about 90°. [214] By changing the composition of the anions (from X = I, Br and Cl), the PL spectrum of $Cs_3Bi_2X_9$ QD shifted from 545 nm to 393 nm, and the PLQY can be significantly enhanced from 0.018% to 26.4% in the UV band.

Chen et al. found UV emission from the transition of free exciton in the 0D metal halide $(C_5H_{14}N_2)_2BiCl_6{\cdot}Cl{\cdot}2\ H_2O$, with the emission peak at 380 nm (Fig. 16**c**). [211] As the temperature decreased from 200 K to

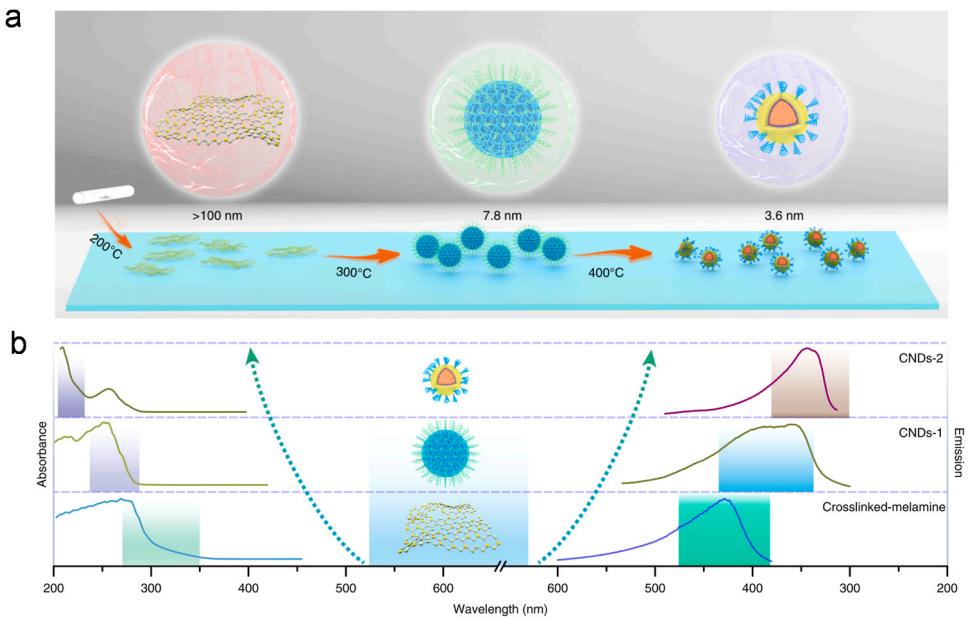

Fig. 12. a. Schematic diagram of the formation mechanism and b. Absorbance and PL emission spectra of the CNDs under different conditions [44]. Copyright 2022.

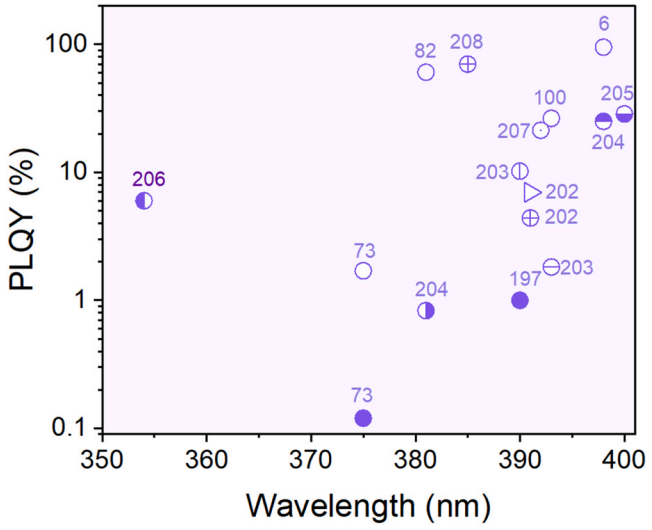

Fig. 13. Peak PLQY of state-of-the-art UV perovskite nanocrystals.

80 K, PL intensity gradually increased, indicating that the thermal quenching effect was suppressed, thus promoting radiation recombination. Sun et al. reported broadband UV emission (392 nm) from 0D perovskite [BAPrEDA]$PbCl_6{\cdot}(H_2O)_2$ radiative transition from a triplet exciton state (Fig. 16**d**). [212] Remarkably, the enhanced quantum confinement of 0D perovskite and the synergistic effect of highly localized excitons significantly increased the PLQY up to 21.3%.

Ion doping is considered as an excellent strategy to extend the luminescence performance of metal halides and to improve PLQY. By heterovalent doping of Cu^+ ions, Zhang et al. prepared Rb_3InCl_6:Cu with highly efficient UV luminescence (398 nm), significantly improved PLQY (95%) and ultra-long lifetime of 13.95 μs (Fig. 16**e**). [6] It's the effective electron isolation, enhanced exciton-phonon coupling, and reasonable electronic structure that creates bright UV emission (Fig. 16**f**).

6. Applications

6.1. Phototherapy

UV is not only positive in regulating the human immune system, but also interacts with human skin tissue for phototherapy. [215] And the intensity, wavelength, and exposure time of light determine the efficacy of phototherapy. [216] The rapid development of UV light sources makes it promising for safe and portable home phototherapy devices.

Especially, NB–UVB (311±2 nm) and broad band UVB (BB–UVB, 300–320 nm) has a long and successful history in the treatment of rickets, skin diseases such as vitiligo [217], psoriasis[218,219] and cutaneous T cell lymphoma [220], as well as graft-versus-host disease [221]. UVA (320–400 nm) is mainly used to treat fibrotic skin conditions such as scleroderma and urticaria pigmentosa, as shown in Fig. 17.

Gd^{3+} is the most popular NB-UVB emitting activating ion. LaB_3O_6:Gd^{3+},Pr^{3+} is a commercial available NB-UVB emitting phosphor for the phototherapy of psoriasis. [222] Moreover, Eu^{2+} activated SrB_4O_7 and $Ba_2B_5O_9Cl$ phosphors have a good effect on the treatment of hyperbilirubinemia as phototherapy lamps. [223]

6.2. Antibacterial and inactivation

UV, especially UVC and UVB (high energy, 3.9–6.2 eV), is capable to kills bacteria and viruses by directly destroying their genetic material (DNA or RNA), thus providing an environmentally friendly, chemical-free method of sterilization. [224] In daily life, antibiotics are the main drugs used to treat daily bacterial diseases. However, the irrational use of antibiotics can lead to serious consequences such as secondary infections, adverse drug reactions, and the development of drug resistance. The use of biomedical engineering equipment such as UV light source is expected to replace or supplement antibiotics in the local treatment of trauma infection, reducing the toxic side effects of drugs and bacterial resistance in humans.

On the other hand, against the backdrop of novel coronavirus pneumonia ravaging the world, the regular disinfection of certain environments and objects in public places such as hospitals and entertainment venues has become inevitable. [224] It is urgent to develop efficient and portable virus disinfection technologies and products to facilitate the regular prevention and control of the epidemic. [225] Mercury lamps are the main source of UV radiation on the market today,

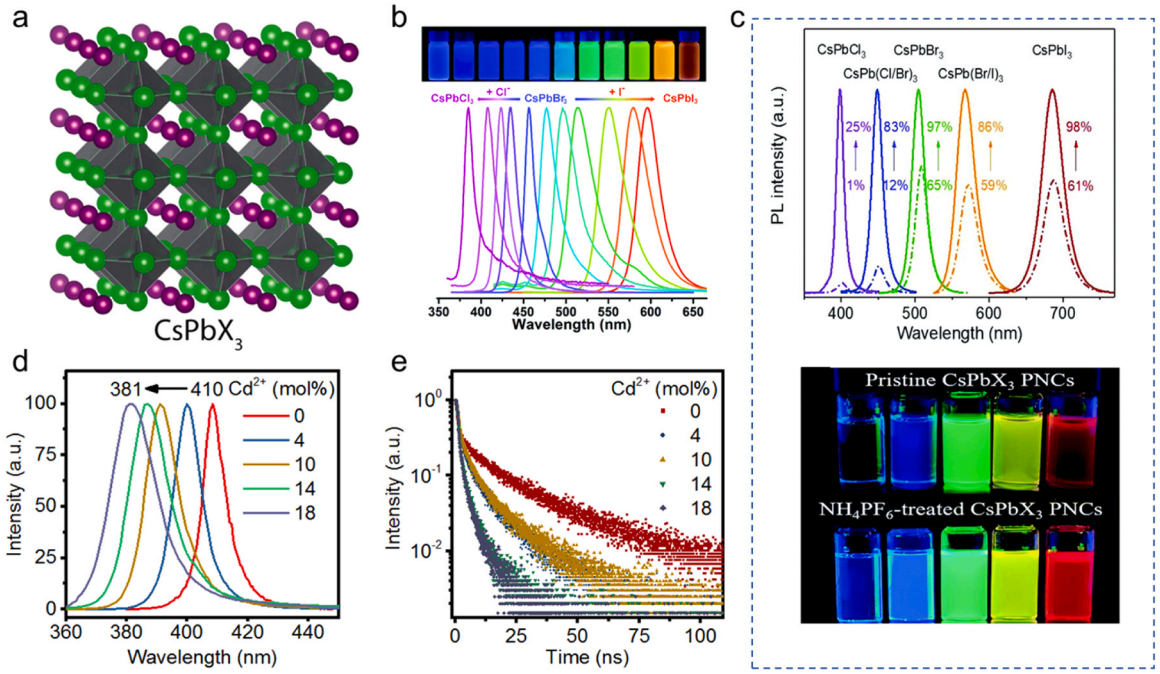

Fig. 14. **a**. Crystal structures of $CsPbX_3$, where purple represents Cs atoms, black Pb atoms, and green Cl/Br/I atoms [198]. Copyright 2017. **b.** Photographs and PL emission spectra of $CsPbX_3$ nanoribbons dispersed in hexane [201]. Copyright 2019. **c.** PL spectra and photographs of $CsPbX_3$ nanocrystals before and after NH_4PF_6-treatment under UV-light (365 nm) excitation [202]. Copyright 2019. **d.** PL spectra, and **e.** PL lifetime of $CsPbCl_3$:Cd^{2+} nanocrystals with different doping concentration of Cd^{2+} [82]. Copyright 2021.

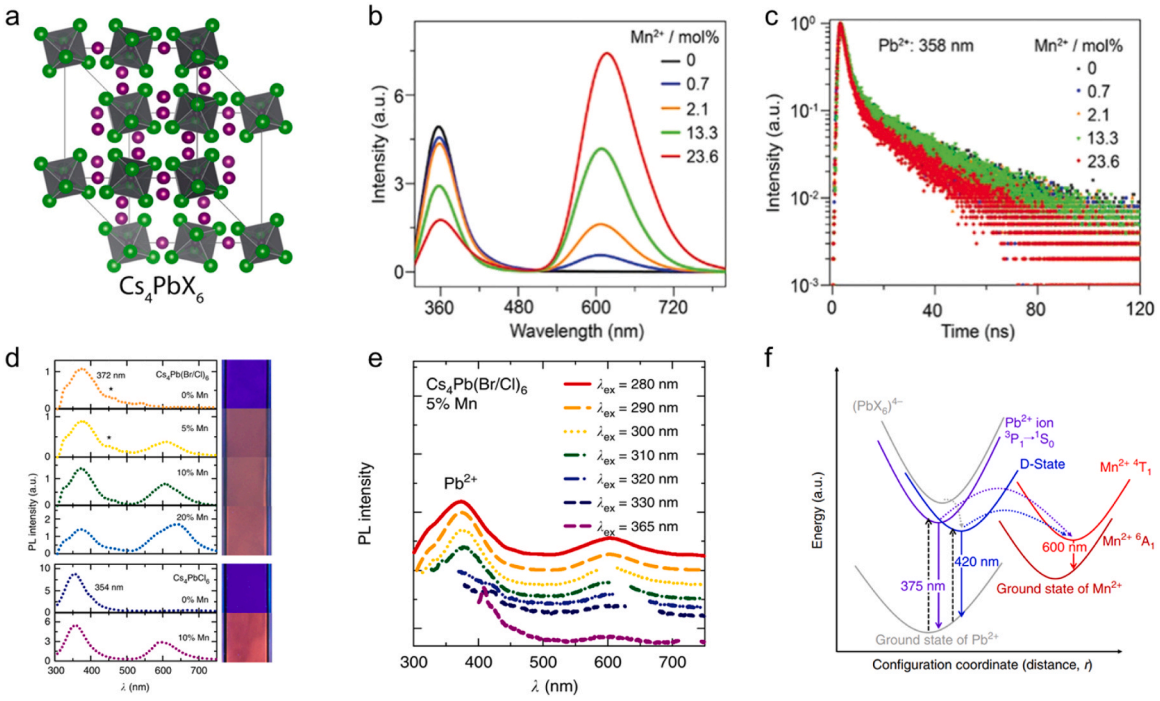

Fig. 15. Crystal structures and luminescent properties of Cs_4PbX_6. a. Crystal structures of Cs_4PbX_6, where purple represents Cs atoms, black Pb atoms, and green Cl/Br/I atoms [198]. Copyright 2017. **b.** PL spectra and **c.** PL lifetime with Mn doping concentration in Cs_4PbCl_6 [206]. Copyright 2020. **d.** PL spectra of Cs_4PbX_6:Mn^{2+} [204]. Copyright 2018. **e.** Excitation-wavelengths-dependent PL of $Cs_4Pb(Br/Cl)_6$:5% Mn [204]. Copyright 2018. **f.** Diagram of energy transfer from Cs_4PbX_6 host states to Mn^{2+} [204]. Copyright 2018.

and are bound to retire due to the Minamata Treaty restricting the use of Hg. [5] Predictably, the new UV luminescent materials provide a strong alternative to commonly used sterilization mercury lamps, opening a new technological path for the development of efficient and cost-effective non-toxic UV solid-state light sources.

UV phosphorescent CNDs can inactivate Gram-negative and Gram-positive bacteria by emitting high-energy photons for a long time, with an antibacterial efficiency of more than 99.9% (as illustrated in

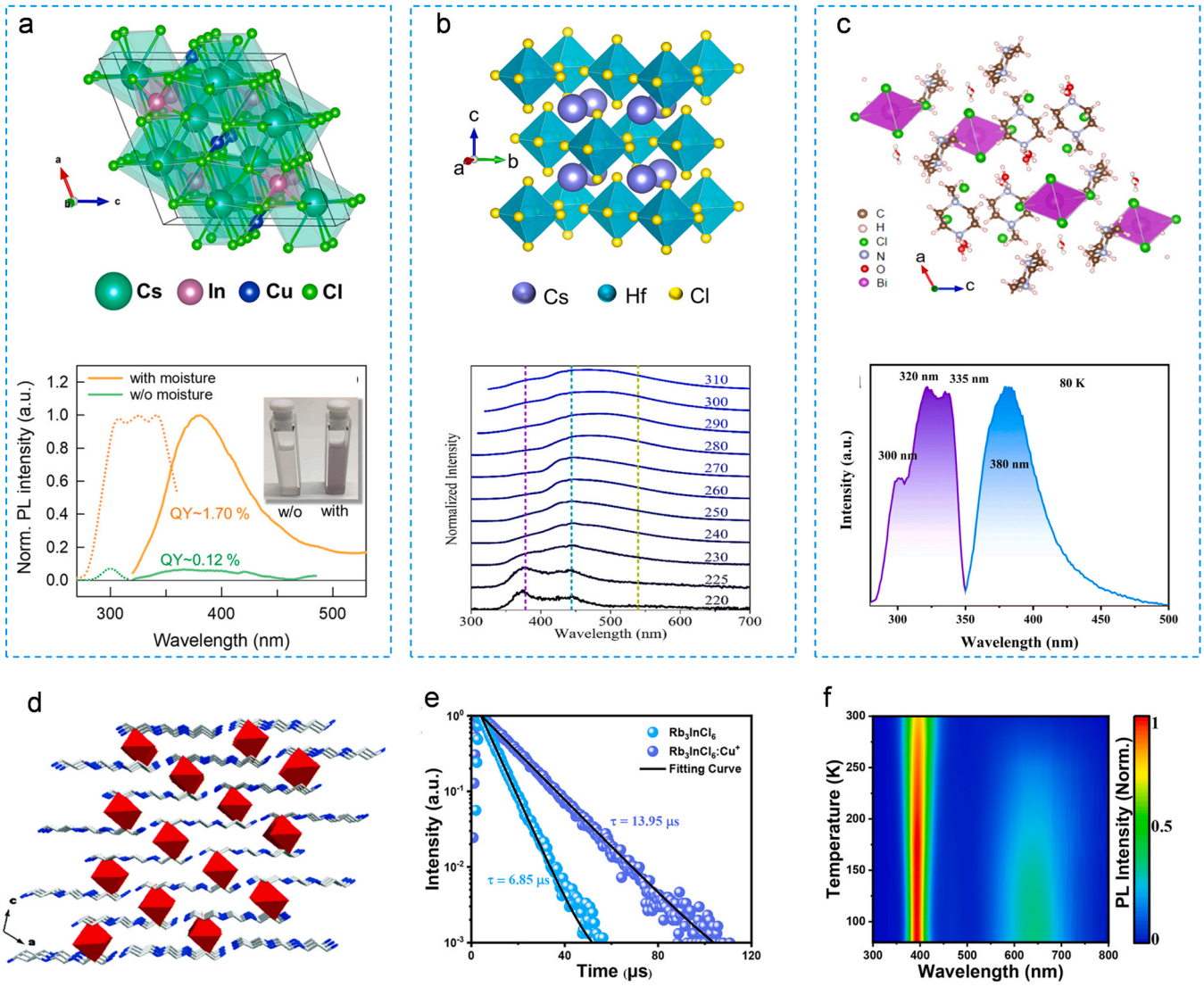

Fig. 16. Crystal structures and luminescent properties of lead-free perovskite. **a.** $Cs_4CuIn_2Cl_{12}$ [58], **b.** Cs_2HfCl_6 [63], **c.** $(C_5H_{14}N_2)_2BiCl_6{\cdot}Cl{\cdot}2\ H_2O$ [211]. Copyright 2022, 2022, and 2023. **d.** $[BAPrEDA]PbCl_6{\cdot}(H_2O)_2$ [212]. Copyright 2022, 2022, 2023, and 2020. **e.** Time-resolved PL and **f.** temperature dependent PL of Rb_3InCl_6: Cu [6]. Copyright 2021.

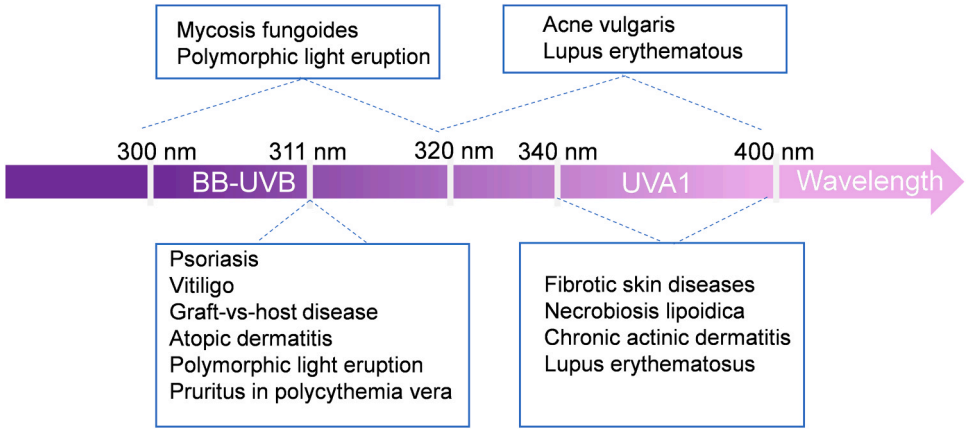

Fig. 17. Phototherapy applications of UV in different wavelengths. Note: Broad-band UVB (BB-UVB).

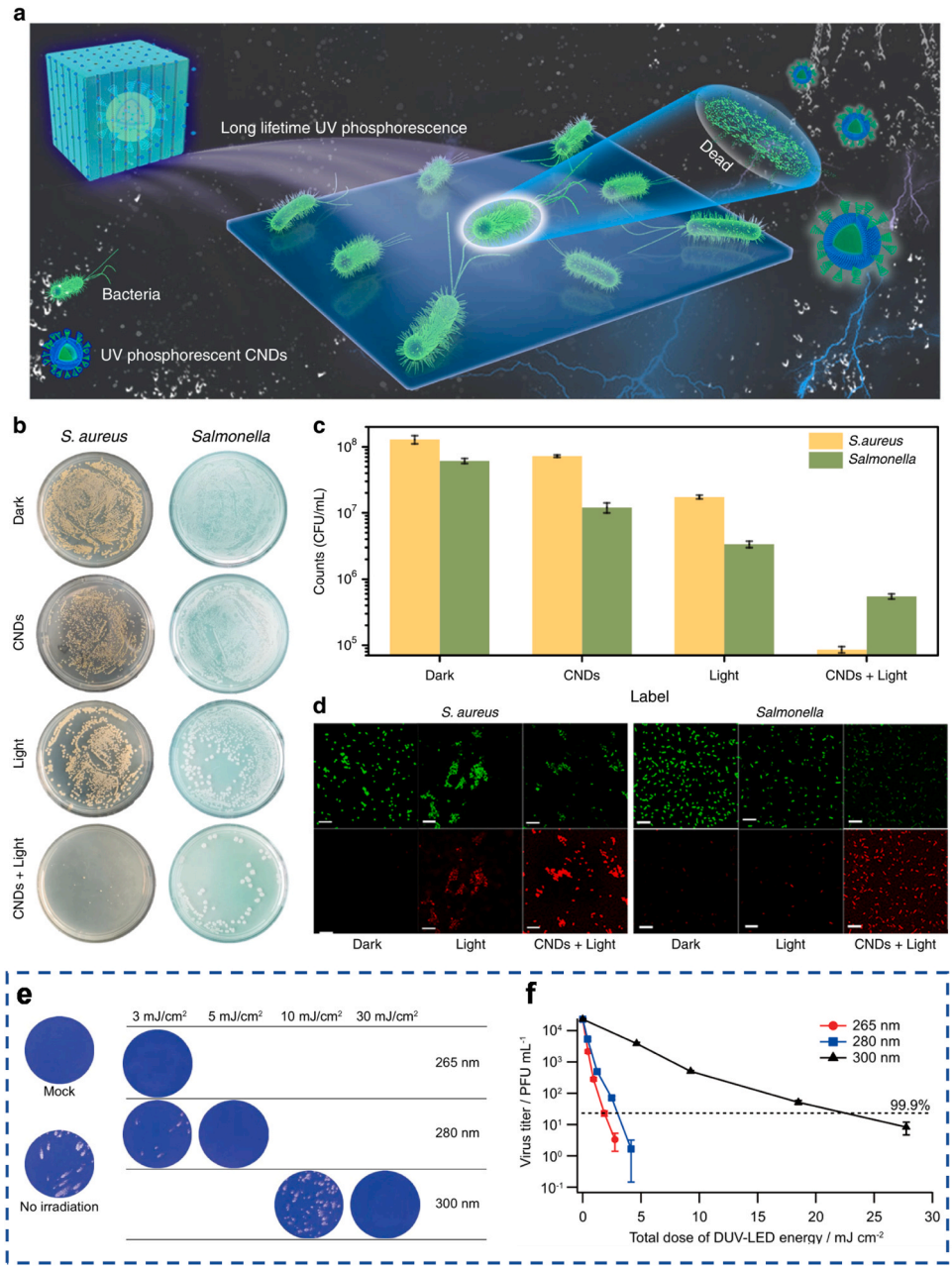

Fig. 18. **a** UV phosphorescence sterilization schematic. **(b)** Images of the colony counting results. **c** Survival statistics of bacteria in panel **b**. **d** CLSM images of *S. aureus* and *Salmonella* after treatment with CNDs-2@NaCNO [52]. Copyright 2022. **e.** Effects of UV-LEDs on SARS-CoV-2 inactivation [226]. Copyright 2021. **f.** Inactivation efficacy of UV-LED with different wavelength [226]. Copyright 2021.

Fig. 18**a**). [44] With the increase of the irradiation period, the death of *S. aureus* and *Salmonella* increased rapidly, and the bacteria showed obvious membrane damage under pulsed light excitation (Fig. 18**b**). After five cycles, the sterilization efficiency can reach 100% (Fig. 18**c**). Confocal laser scanning microscope (CLSM) images also show the high antibacterial activity of CNDs (Fig. 18**d**). Xia et al. also demonstrated a combination of blue light stimulated UV phosphors in inactivating Staphylococcus aureus. [130]

Due to the broad-spectrum nature of UV, UV light-emitting diodes (UV-LED) are promising candidates for inactivating SARS-CoV-2, which is the beta coronavirus causing COVID-19. [227] Griffiths et al. demonstrated that the use of UVC-LED (280 nm, 3.75 mW/cm^2) could inactivate SARS-CoV-2 in wet droplets within 10 s. [228] A recent study showed that both wet and dry forms of SARS-CoV-2 could be rapidly (4–9 s) and completely inactivated using a commercially available Signify UVC light source (254 nm, 0.849 mW/cm^2). [229]

Nomaguchi et al. also investigated the SARS-CoV-2 inactivation efficacy by different wavelengths of UV-LED (265, 280 and 300 nm). [226] The results indicated that the dose of UV at each wavelength could lead to a decrease in the infectivity of SARS-CoV-2 (Fig. 18**e**). Moreover, UV at 265 nm was most effective in inactivating SARS-CoV-2, due to the strong absorption of viral RNA at 265 nm (Fig. 18**f**).

Buonanno et al. demonstrated that using far-UVC-LED (222 nm) to kill inactivates human coronaviruses results in ~90% virus inactivation within ~8 minutes and ~ 99.9% inactivation within 25 minutes, at a sustained exposure limit of 3 mJ/cm^2/hour in occupied public Spaces. [230] This strongly demonstrates that low doses of UV can safely substantially reduce environmental levels of coronavirus in public places. The above studies show that UV has great potential in bactericidal and antibacterial applications.

6.3. Plant lighting

Different wavelengths of UV light have different regulatory effects on plant growth and development, and plants receive different wavelengths of light through specific photoreceptors: phototropin and Zeitlupes family proteins receive UVA light signals, and UVR8 (UVResistanceLocus8) protein receives UVB light signals. [231,232] The response of plants to UVB light is affected by light intensity, wavelength and duration of exposure. [233] UVB radiation is a key environmental signal affecting plant growth and development, and UVB with appropriate intensity and wavelength positively regulates various developmental processes in plants, such as photomorphogenesis, shade avoidance, phototropism, and leaf growth and development.[234] A growing body of research supports supplementing UVB radiation in sustainable crop production.

Fig. 19**a** displays the effect of different UV light treatments on the growth of basil over 10 days. [48] Among them, UVB LED is composed of solid-state CDs emitting UVB and LED chip for plant lighting. By comparing the content of chlorophyll and carotenoid, it was found that UVB irradiation had no significant damage to the photosynthetic system of plants (Fig. 19**b-c**). Interestingly, UVB exposure increased ascorbic acid content and anthocyanin levels in basil by 29% and 35%, respectively (Fig. 19**d**). It has also been shown that UVB irradiation promoted the conversion of 7-dehydrocholesterol into vitamin D_3 in tomato plants. [235]

6.4. Imaging and anti-counterfeiting

The persistent luminescence UVC afterglow compensates for application scenarios that cannot be realized with visible persistent phosphors. It's a zero-background condition of UVC in atmosphere. so it's easy to monitor and record artificial UVC radiation, such as power company discharge, during the day and night using a high-contrast and equally effective UVC coronal camera.

Wang et al. used $Ca_2Al_2SiO_7:Pr^{3+}$ UVC persistent phosphors as a self-luminous solar-blind tag, achieving high-contrast sensitive monitoring in bright environment. [5] Fig. 20**a** shows that the uncharged white $Ca_2Al_2SiO_7:Pr^{3+}$ disc with a diameter of 50 mm is virtually indistinguishable from the white plate when viewed from a distance of about 8 m under direct sunlight. However, the corona camera clearly detects the intense UV afterglow radiation of $Ca_2Al_2SiO_7:Pr^{3+}$ disc and image in direct sunlight for up to 2 hours (Fig. 20**b-d**). UVC radiation is extinguished for coronal camera as the decay time exceeds 2 hours. Under direct sunlight, UVC are also detected on a 20 mm diameter disk (Fig. 20**e, f**) and paint made of a powder mixture (Fig. 20**g, h**). Liu et al. used UVB persistent luminescence in the $Mg_2Lu_2Ge_3O_{11}:Bi^{3+}$ (MLG) to achieve highly concealed digital encryption, quick response (QR) code encryption, and trademark encryption. It can be seen that UV light with unique advantages have great potential in advanced anti-counterfeiting (Fig. 20**i**). [144]

6.5. Other applications

In addition to these several promising applications mentioned above, UV luminescent materials also have important applications in photo curing and photocatalysis. The technology of curing resins with UV luminescent materials has been applied in the field of medical-surgical, dental or implant applications, as well as in 3D printing technology. [236] The UV-emitting material $K_2YbF_5:Tm^{3+}$ is used to cure photosensitive resins due to the fact that its emission energy is fully compatible with the activation energy of the photosensitive resin.

UV light also provides a unique approach to access the excited states in photocatalytic technology. And the excited states can be reached by lower energy radiation under the action of photosensitizer. [237] TiO_2 is one of the most popular commercial photocatalysts. It is a wide-band gap semiconductor oxide photocatalyst, which is only effective for photocatalysis under UV irradiation. [238] $Zn_2SiO_4:Ga^{3+}$, Bi^{3+} UV long afterglow material developed by Mei et al. can be used as an additional light source to promote TiO_2 photocatalysis in dark environment.[239] The researchers also investigated the effect of UV on the degradation of

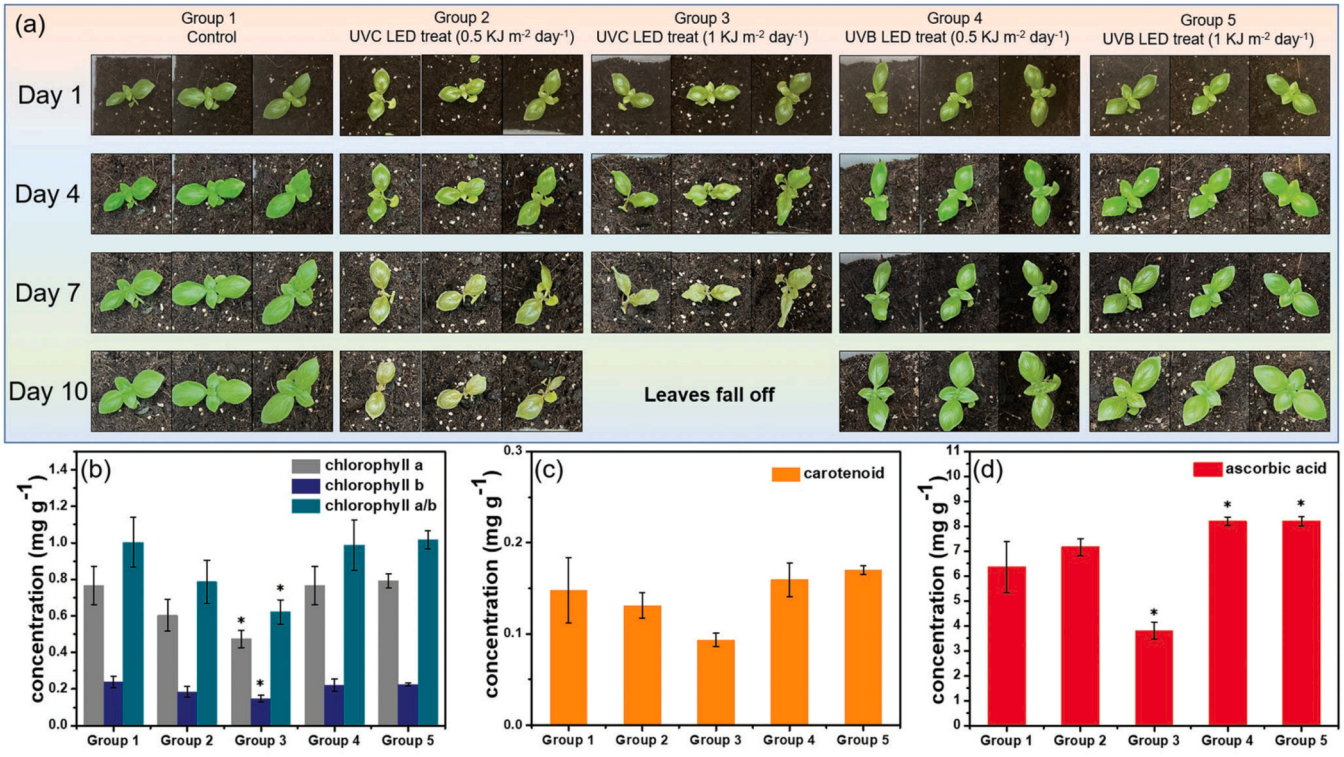

Fig. 19. UV light as plant lighting. a. Effects of different UV light combinations on the growth of basil. The **b** chlorophyll, **c** carotenoid, and **d** ascorbic acid content of different groups of basil [48]. Copyright 2022.

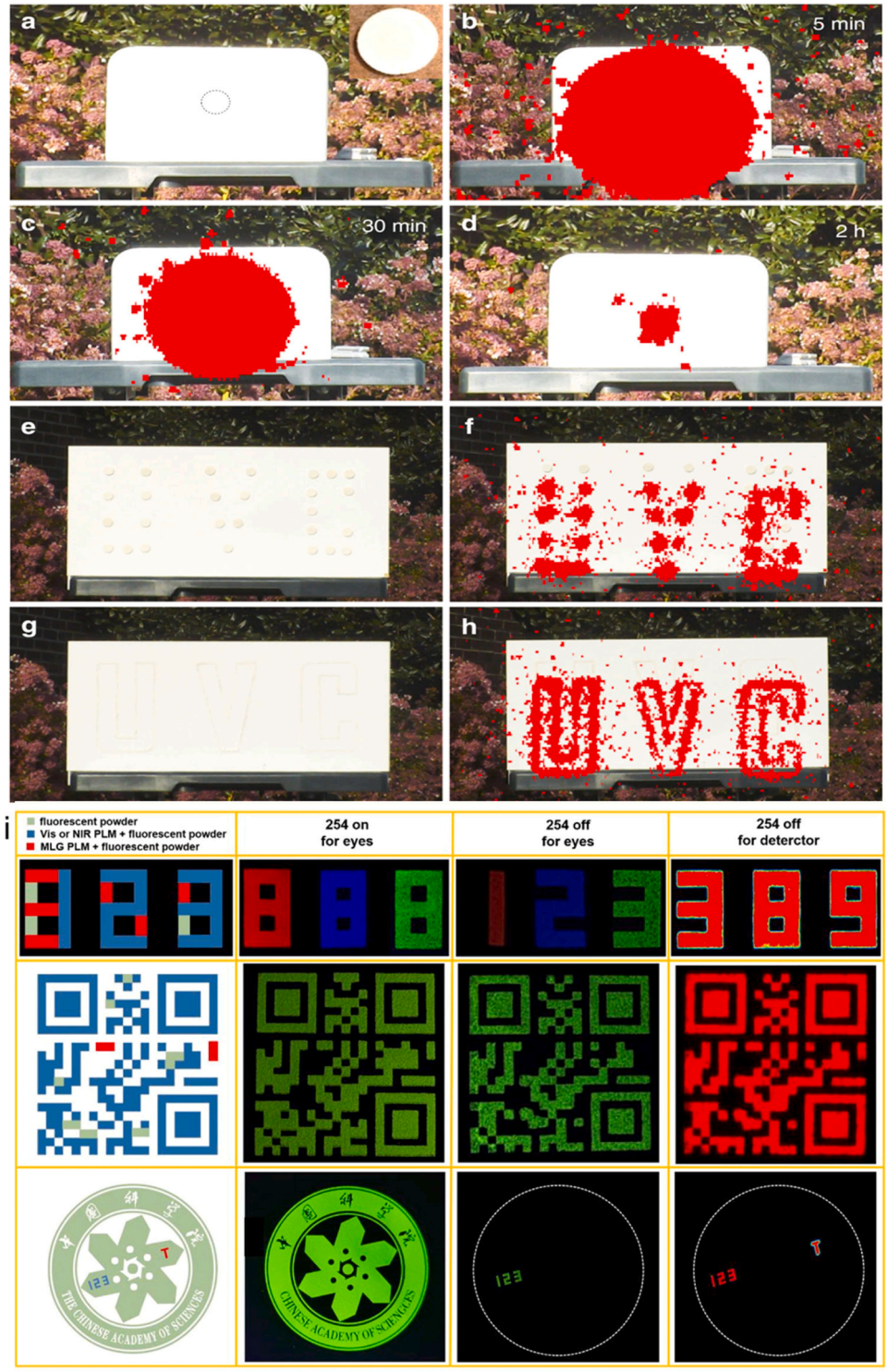

Fig. 20. UV light for imaging and anti-counterfeiting. a. $Ca_2Al_2SiO_7:Pr^{3+}$ white-color disc. **b–d.** UVC images of the discs taken using a corona camera. Image of letters "U", "V", and "C" **e** and paint **g** on a white wood board. UVC image of the disc letters **f** and paint letters **h** [5]. Copyright 2020. **i.** Strategy for designing anti-counterfeiting under different conditions for digital encryption, QR code encryption, and trademark encryption [144]. Copyright 2022.

toxic compounds such as phenol and naphthalene. [240,241]

7. Conclusions and outlook

Overall, almost all kinds of luminescent materials, including carbon dot-based nanomaterials, perovskite nanocrystals as well as rare earth or main group metal ion-activated phosphors have come a long way in just two decades. The highest reported PLQY value has exceeded 95% at 398 nm. The rapid development of chip technology and the successful application cases of visible and NIR light-emitting materials will inevitably accelerate the rapid rise of UV luminescent materials and devices at the other end of the spectrum, in order to make these materials or devices more energy-efficient and cost-effective. However, there are still many challenges that need to be addressed to move UV luminescent

materials from the laboratory to practical applications.

The first is higher PLQY and longer lifetime. Despite the much higher PLQY values reported, there are still fewer materials with UVC regional emission and, more importantly, the efficiency needs to be improved. The integration of novel perovskite or CDs emitters into LEDs is not yet mature. [242] Currently developed perovskite, despite their high quantum efficiency, are not yet suitable for applications such as disinfectants and water sterilization because the emission wavelength does not yet reach the UVC band.

The second is UV safety. UV light is a double-edged sword, the correct and reasonable use of UV light will have a positive effect on human health and disease treatment. However, improper use will irritate the mucous membranes of the skin and the eyes, causing harm to the human body. Therefore, it is necessary to establish a correct awareness of UV safety. At the same time, it can be combined with advanced technologies such as sterilization robots to reduce direct contact with humans.

Finally, faster research and development process. At this stage, UV luminescent materials mainly rely on a lot of trial and error process to develop new materials. There is a lack of rational material design principles and faster screening methods. Therefore, screening of material components with the help of high-throughput computation and high-throughput experiments will greatly accelerate the process of material development. Designing UV materials based on computational models of quantum chemistry or artificial intelligence techniques such as machine learning may be a promising research direction.

The rapid discovery and extensive research on the mechanisms of UV luminescence will certainly solve many of these challenges. At the same time, the integration of machine learning and high-throughput experimental synthesis has great potential to accelerate research on UV luminescent materials. [243,244] Unveiling the mystery of UV will broaden the scope of their applications, so that UV light source can enter the life of ordinary people like lighting source.

CRediT authorship contribution statement

Yun Shi: Writing – review & editing, Supervision. **Yanjie Liang:** Writing – review & editing, Supervision, Investigation. **Junfeng Chen:** Writing – review & editing, Conceptualization. **Mingxue Deng:** Writing – original draft, Investigation, Conceptualization. **Qian Liu:** Writing – review & editing, Supervision, Conceptualization. **Jiacheng Wang:** Writing – review & editing, Investigation.

Declaration of Competing Interest

The authors declare that they have no known competing financial interests or personal relationships that could have appeared to influence the work reported in this paper.

Data Availability

No data was used for the research described in the article.

Acknowledgments

Junfeng Chen would like to acknowledge National Key Program for S&T Research and Development (grant number 2023YFA1606300), the Strategic Priority Research Program of the Chinese Academy of Sciences (grant number XDA25030600), and the Natural Science Foundation of China (grant number U1867211).

References

[1] S. Chen, H. Xu, Chem. Soc. Rev. 50 (2021) 8639–8668.
[2] D.S. Thakare, S.K. Omanwar, P.L. Muthal, S.M. Dhopte, V.K. Kondawar, S. V. Moharil, Phys. Status Solidi (a) 201 (2004) 574–581.
[3] C. Zhu, S. Yang, J. Sun, P. He, N. Yuan, J. Ding, R. Mo, G. Wang, G. Ding, X. Xie, Synth. Met. 209 (2015) 468–472.
[4] L. Tang, R. Ji, X. Cao, J. Lin, H. Jiang, X. Li, K.S. Teng, C.M. Luk, S. Zeng, J. Hao, S.P. Lau, ACS Nano 6 (2012) 5102–5110.
[5] X. Wang, Y. Chen, F. Liu, Z. Pan, Nat. Commun. 11 (1) (2020) 2040.
[6] C. Zhang, X. Feng, Q. Song, C. Zhou, L. Peng, J. Chen, X. Liu, H. Chen, J. Lin, X. Chen, J. Phys. Chem. Lett. 12 (2021) 7928–7934.
[7] X. Wang, Y. Mao, J. Mater. Chem. C. 10 (2022) 3626–3646.
[8] X. Wang, Y. Mao, Adv. Opt. Mater. 10 (2022) 2201466.
[9] Y. Zhang, Y. Liang, X. Shan, D. Chen, S. Miao, R. Shi, F. Xie, W. Wang, Inorg. Chem. 61 (2022) 20647–20656.
[10] J.T.W. de Hair, J. Lumin 18-19 (1979) 797–800.
[11] N.S.B.P.A. Nagpure, R.P. Sonekar, S.K. Omanwar, Indian J. Pure Appl. Phys. 49 (2011) 799–802.
[12] X. Wang, Y. Mao, Adv. Opt. Mater. 10 (2022) 2102157.
[13] P. Dang, D. Liu, G. Li, A.A. Al Kheraif, J. Lin, Adv. Opt. Mater. 8 (2020) 1901993.
[14] X. Wang, C. Heng, Z. Qiao, L. Ning, J. Lumin 244 (2022) 118700.
[15] E.L. Cates, J.-H. Kim, Opt. Mater. 35 (2013) 2347–2351.
[16] Q. Su, H.-L. Wei, Y. Liu, C. Chen, M. Guan, S. Wang, Y. Su, H. Wang, Z. Chen, D. Jin, Nat. Commun. 12 (2021) 4367.
[17] J. Li, L. Wang, Z. Zhao, B. Sun, G. Zhan, H. Liu, Z. Bian, Z. Liu, Nat. Commun. 11 (2020) 5218.
[18] J.-C. Rybak, M. Hailmann, P.R. Matthes, A. Zurawski, J. Nitsch, A. Steffen, J. G. Heck, C. Feldmann, S. Götzendörfer, J. Meinhardt, G. Sextl, H. Kohlmann, S. J. Sedlmaier, W. Schnick, K. Müller-Buschbaum, J. Am. Chem. Soc. 135 (2013) 6896–6902.
[19] G. Blasse, B.C. Grabmaier, Radiative Return to the Ground State: Emission, in: G. Blasse, B.C. Grabmaier (Eds.), Luminescent Materials, Springer Berlin Heidelberg, Berlin, Heidelberg, 1994, pp. 33–70.
[20] Y. Tang, M. Deng, M. Wang, X. Liu, Z. Zhou, J. Wang, Q. Liu, Advanced, Opt. Mater. (2022) 2201827.
[21] R.H.P. Awater, P. Dorenbos, J. Lumin 184 (2017) 221–231.
[22] Z. Feng, B. Lou, M. Yin, Y.-y Yeung, H.-T. Sun, C.-K. Duan, Inorg. Chem. 60 (2021) 4434–4446.
[23] E.L. Cates, S.L. Chinnapongse, J.-H. Kim, J.-H. Kim, Environ. Sci. Technol. 46 (2012) 12316–12328.
[24] X. Cheng, J. Zhou, J. Yue, Y. Wei, C. Gao, X. Xie, L. Huang, Chem. Rev. 122 (2022) 15998–16050.
[25] J. Wu, H. Zheng, X. Liu, B. Han, J. Wei, Y. Yang, Opt. Lett. 41 (2016) 792–795.
[26] P. Lv, L. Li, C. Wang, Z. Wu, J. Qiu, Y. Yang, Laser Photonics Rev. 16 (2022) 2200389.
[27] E.L. Cates, F. Li, RSC Adv. 6 (2016) 22791–22796.
[28] S. Tamboli, S.J. Dhoble, SPECTROCHIMICA ACTA PART A-Mol. BIOMOLECULAR Spectrosc. 184 (2017) 119–127.
[29] Y. Liu, M. Zhou, M.-T. Zhou, H.-L. Wei, Y. Su, Q. Su, Nanoscale 14 (2022) 4595–4603.
[30] H.-L. Wei, W. Zheng, X. Zhang, H. Suo, B. Chen, Y. Wang, F. Wang, Adv. Opt. Mater. 11 (2023) 2201716.
[31] S. Tao, C. Zhou, C. Kang, S. Zhu, T. Feng, S.-T. Zhang, Z. Ding, C. Zheng, C. Xia, B. Yang, Light.: Sci. Appl. 11 (2022) 56.
[32] D.A.M. Muyassiroh, F.A. Permatasari, F. Iskandar, J. Mater. Chem. C. 10 (2022) 17431–17450.
[33] F. Yuan, Z. Wang, X. Li, Y. Li, Za Tan, L. Fan, S. Yang, Adv. Mater. 29 (2017) 1604436.
[34] C. Xia, S. Zhu, T. Feng, M. Yang, B. Yang, Adv. Sci. 6 (2019) 1901316.
[35] Y. Zhai, B. Zhang, R. Shi, S. Zhang, Y. Liu, B. Wang, K. Zhang, G.I.N. Waterhouse, T. Zhang, S. Lu, Adv. Energy Mater. 12 (2022) 2103426.
[36] Q. Zhao, W. Song, B. Zhao, B. Yang, Mater. Chem. Front. 4 (2020) 472–488.
[37] C. Tang, Q. Zhang, Adv. Mater. 29 (2017) 1604103.
[38] Q. Zhang, R. Wang, B. Feng, X. Zhong, K. Ostrikov, Nat. Commun. 12 (2021) 6856.
[39] S. Li, L. Li, H. Tu, H. Zhang, D.S. Silvester, C.E. Banks, G. Zou, H. Hou, X. Ji, Mater. Today 51 (2021) 188–207.
[40] Y. Yan, J. Chen, N. Li, J. Tian, K. Li, J. Jiang, J. Liu, Q. Tian, P. Chen, ACS Nano 12 (2018) 3523–3532.
[41] S.-Y. Song, K.-K. Liu, J.-Y. Wei, Q. Lou, Y. Shang, C.-X. Shan, Nano Lett. 19 (2019) 5553–5561.
[42] F. Yuan, Y.-K. Wang, G. Sharma, Y. Dong, X. Zheng, P. Li, A. Johnston, G. Bappi, J.Z. Fan, H. Kung, B. Chen, M.I. Saidaminov, K. Singh, O. Voznyy, O.M. Bakr, Z.-H. Lu, E.H. Sargent, Nat. Photonics 14 (2020) 171–176.
[43] M.-J. Yang, J.-X. Shi, Y. Yin, C.-G. Shi, Phys. Status Solidi (b) 258 (2021) 2100110.
[44] S.-Y. Song, K.-K. Liu, Q. Cao, X. Mao, W.-B. Zhao, Y. Wang, Y.-C. Liang, J.-H. Zang, Q. Lou, L. Dong, C.-X. Shan, Light.: Sci. Appl. 11 (2022) 146.
[45] T. Kim, K.-H. Kim, S. Kim, S.-M. Choi, H. Jang, H.-K. Seo, H. Lee, D.-Y. Chung, E. Jang, Nature 586 (2020) 385–389.
[46] X. Yan, X. Yao, Defective Carbons for Electrocatalytic Oxygen Reduction, Carbon-Based Metal-Free Catalysts, Wiley-VCH Verlag GmbH & Co. KGaA, Hoboken, New Jersey, 2018, pp. 59-75.
[47] J.E. Abraham, M. Balachandran, J. Fluoresc. 32 (2022) 887–906.
[48] J. Xu, Q. Liang, Z. Li, V.Y. Osipov, Y. Lin, B. Ge, Q. Xu, J. Zhu, H. Bi, Adv. Mater. 34 (2022) 2200011.
[49] S. Liu, X. Fang, B. Lu, D. Yan, Nat. Commun. 11 (2020) 4649.
[50] Y. Sun, S. Liu, L. Sun, S. Wu, G. Hu, X. Pang, A.T. Smith, C. Hu, S. Zeng, W. Wang, Y. Liu, M. Zheng, Nat. Commun. 11 (2020) 5591.
[51] Y. Deng, D. Zhao, X. Chen, F. Wang, H. Song, D. Shen, Chem. Commun. (Camb., U. K.) 49 (2013) 5751–5753.

[52] H. Wang, Y. Zhang, C. Zhou, X. Wang, H. Ma, J. Yin, H. Shi, Z. An, W. Huang, Light.: Sci. Appl. 12 (2023) 90.
[53] J. Nie, B. Zhou, S. Fang, Y. Wang, Y. Wang, B. Tian, H. Hu, H. Zhong, H. Li, Y. Shi, Mater. Today Phys. 31 (2023) 100992.
[54] H.F. Folkerts, A.V. Dijken, G. Blasse, J. Phys.: Condens. Matter 7 (1995) 10049.
[55] H.C. Swart, R.E. Kroon, Opt. Mater.: X 2 (2019) 100025.
[56] J. Yin, Y. Zhang, A. Bruno, C. Soci, O.M. Bakr, J.-L. Brédas, O.F. Mohammed, ACS Energy Lett. 2 (2017) 2805–2811.
[57] Z. Gao, P. Lyu, C. Xu, L. Sun, Chem. Eng. J. 458 (2023) 141533.
[58] M. Liu, S.K. Matta, H. Ali-Löytty, A. Matuhina, G.K. Grandhi, K. Lahtonen, S. P. Russo, P. Vivo, Nano Lett. 22 (2022) 311–318.
[59] J. Luo, X. Wang, S. Li, J. Liu, Y. Guo, G. Niu, L. Yao, Y. Fu, L. Gao, Q. Dong, C. Zhao, M. Leng, F. Ma, W. Liang, L. Wang, S. Jin, J. Han, L. Zhang, J. Etheridge, J. Wang, Y. Yan, E.H. Sargent, J. Tang, Nature 563 (2018) 541–545.
[60] H.F. Folkerts, F. Ghianni, G. Blasse, J. Phys. Chem. Solids 57 (1996) 1659–1665.
[61] A. Burger, E. Rowe, M. Groza, K. Morales Figueroa, N.J. Cherepy, P.R. Beck, S. Hunter, S.A. Payne, Appl. Phys. Lett. 107 (2015) 143505.
[62] K. Saeki, Y. Fujimoto, M. Koshimizu, T. Yanagida, K. Asai, Appl. Phys. Express 9 (2016) 042602.
[63] S. Liu, B. Yang, J. Chen, D. Zheng, Z. Tang, W. Deng, K. Han, Laser Photonics Rev. 16 (2022) 2100439.
[64] K. Tanaka, T. Takahashi, T. Kondo, K. Umeda, K. Ema, T. Umebayashi, K. Asai, K. Uchida, N. Miura, Jpn. J. Appl. Phys. 44 (2005) 5923.
[65] T. Ishihara, J. Lumin 60-61 (1994) 269–274.
[66] N. Kitazawa, Mater. Sci. Eng.: B 49 (1997) 233–238.
[67] R.K. Misra, B.-E. Cohen, L. Iagher, L. Etgar, ChemSusChem 10 (2017) 3712–3721.
[68] I. Neogi, A. Bruno, D. Bahulayan, T.W. Goh, B. Ghosh, R. Ganguly, D. Cortecchia, T.C. Sum, C. Soci, N. Mathews, S.G. Mhaisalkar, ChemSusChem 10 (2017) 3765–3772.
[69] P. Cai, Y. Huang, H.J. Seo, J. Phys. Chem. Lett. 10 (2019) 4095–4102.
[70] M.D. Smith, H.I. Karunadasa, Acc. Chem. Res. 51 (2018) 619–627.
[71] E. Hanamura, N. Nagaosa, M. Kumagai, T. Takagahara, Mater. Sci. Eng.: B 1 (1988) 255–258.
[72] M.D. Smith, L. Pedesseau, M. Kepenekian, I.C. Smith, C. Katan, J. Even, H. I. Karunadasa, Chem. Sci. 8 (2017) 1960–1968.
[73] F. Jiang, Z. Wu, M. Lu, Y. Gao, X. Li, X. Bai, Y. Ji, Y. Zhang, Adv. Mater. (2023) 2211088 (n/a).
[74] T. Hu, M.D. Smith, E.R. Dohner, M.-J. Sher, X. Wu, M.T. Trinh, A. Fisher, J. Corbett, X.Y. Zhu, H.I. Karunadasa, A.M. Lindenberg, J. Phys. Chem. Lett. 7 (2016) 2258–2263.
[75] L. Mao, Y. Wu, C.C. Stoumpos, B. Traore, C. Katan, J. Even, M.R. Wasielewski, M. G. Kanatzidis, J. Am. Chem. Soc. 139 (2017) 11956–11963.
[76] M.D. Smith, A. Jaffe, E.R. Dohner, A.M. Lindenberg, H.I. Karunadasa, Chem. Sci. 8 (2017) 4497–4504.
[77] Q. Guo, X. Zhao, B. Song, J. Luo, J. Tang, Adv. Mater. 34 (2022) 2201008.
[78] C. Zhou, H. Lin, Y. Tian, Z. Yuan, R. Clark, B. Chen, L.J. van de Burgt, J.C. Wang, Y. Zhou, K. Hanson, Q.J. Meisner, J. Neu, T. Besara, T. Siegrist, E. Lambers, P. Djurovich, B. Ma, Chem. Sci. 9 (2018) 586–593.
[79] Z.-J. Yong, S.-Q. Guo, J.-P. Ma, J.-Y. Zhang, Z.-Y. Li, Y.-M. Chen, B.-B. Zhang, Y. Zhou, J. Shu, J.-L. Gu, L.-R. Zheng, O.M. Bakr, H.-T. Sun, J. Am. Chem. Soc. 140 (2018) 9942–9951.
[80] J. Pan, Z. Zhao, F. Fang, L. Wang, G. Wang, C. Liu, J. Chen, J. Xie, J. Sun, K. Wang, X. Liu, Z. Tao, J. Zhao, Q. Wu, J. Chang, Y. Wang, W. Lei, W. Zhang, X. W. Sun, D. Zhao, Adv. Opt. Mater. 8 (2020) 2001494.
[81] N. Mondal, A. De, A. Samanta, ACS Energy Lett. 4 (2019) 32–39.
[82] Y. Zhang, X. Cheng, D. Tu, Z. Gong, R. Li, Y. Yang, W. Zheng, J. Xu, S. Deng, X. Chen, Angew. Chem. Int. Ed. 60 (2021) 9693–9698.
[83] V. Singh, S. Kaur, A.S. Rao, N. Singh, J.L. Rao, M. Irfan, Optik 206 (2020) 164263.
[84] V. Singh, S. Kaur, A.S. Rao, N. Singh, M.S. Pathak, J.L. Rao, J. Electron. Mater. 48 (2019) 4092–4098.
[85] V. Singh, A. Prasad, A.S. Rao, S.W. Jung, N. Singh, M. Irfan, Optik 225 (2021) 165442.
[86] V. Singh, B.R. Venkateswara Rao, A.S. Rao, J.L. Rao, M. Irfan, Optik 206 (2020) 164020.
[87] T. Deng, S. Yan, J. Hu, J. Rare Earths 34 (2016) 137–142.
[88] A.O. Chauhan, A.B. Gawande, S.K. Omanwar, Optik 127 (2016) 6647–6652.
[89] A.O. Chauhan, A.B. Gawande, S.K. Omanwar, Mater, J. Inorg. Organomet. Polym. 26 (2016) 1023–1027.
[90] V. Singh, C.B. Annapurna Devi, A.S. Rao, J.L. Rao, Optik 208 (2020) 163632.
[91] V. Singh, V.P. Singh, N. Singh, H. Jeong, V. Natarajan, Radiat. Phys. Chem. 174 (2020).
[92] R.G. Kunghatkar, V.L. Barai, S.J. Dhoble, Results Phys. 13 (2019) 102295.
[93] D. Yang, Y. Zheng, Z. Fang, J. Zhu, Mater. Today Commun. 33 (2022) 104697.
[94] Z. Yu, Y. Yang, J. Sun, Nanomaterials 13 (2023) 1013.
[95] A.B. Gawande, R.P. Sonekar, S.K. Omanwar, Mater. Res. Bull. 60 (2014) 285–291.
[96] S.P. Bhagat, A.B. Gawande, S.K. Omanwar, Opt. Mater. 40 (2015) 36–40.
[97] R.P. Sonekar, S.K. Omanwar, S.V. Moharil, S.M. Dhopte, P.L. Muthal, V. K. Kondawar, Opt. Mater. 30 (2007) 622–625.
[98] A.B. Gawande, R.P. Sonekar, S.K. Omanwar, Optik 127 (2016) 3925–3927.
[99] D. Yu, H. Li, D. Zhang, Q. Zhang, A. Meijerink, M. Suta, Light.: Sci. Appl. 10 (2021) 236.
[100] A.O. Chauhan, N.S. Bajaj, S.K. Omanwar, Bull. Mater. Sci. 40 (2017) 1–6.
[101] V. Singh, G. Sivaramaiah, N. Singh, M.S. Pathak, A.K. Srivastava, J.L. Rao, V. Natarajan, Optik 171 (2018) 552–556.
[102] V. Singh, N. Singh, M.S. Pathak, V. Natarajan, N.A. Jadhav, Optik 176 (2019) 650–654.
[103] M.S. Pathak, N. Singh, V. Singh, S. Watanabe, T.K. Gundu Rao, M. Seshadri, J.-K. Lee, J. Lumin 204 (2018) 75–80.
[104] V. Singh, N. Singh, M.S. Pathak, V. Natarajan, J. Electron. Mater. 48 (2019) 238–243.
[105] V. Singh, N. Singh, M.S. Pathak, S. Watanabe, T.K.G. Rao, P.K. Singh, V. Dubey, Optik 157 (2018) 1391–1396.
[106] X. Zhao, F. Liu, X.-j Wang, Y. Liu, Phys. Rev. Appl. 15 (2021) 064039.
[107] V. Singh, N. Singh, M.S. Pathak, S. Watanabe, T.K.G. Rao, P.K. Singh, Y.-W. Kwon, J. Mater. Sci. -Mater. Electron. 29 (2018) 4632–4638.
[108] B. Yin, P. Lv, Y. Yang, L. Li, J. Appl. Phys. 132 (2022).
[109] V. Singh, A. Yadav, A.S. Rao, N. Singh, J.L. Rao, M. Irfan, Optik 225 (2021) 165442.
[110] V. Singh, N. Singh, M.S. Pathak, V. Natarajan, J. Electron. Mater. 48 (2019) 1498–1505.
[111] A.A. Sharma, M. Rakshita, P.P. Pradhan, K.A.K. Durga Prasad, S. Mishra, K. Jayanthi, D. Haranath, J. Mater. Res. 38 (2023) 2812–2822.
[112] V. Singh, S. Kaur, A.S. Rao, J.L. Rao, M. Irfan, Optik 204 (2020) 164475.
[113] V. Singh, R. Bajaj, S. Kaur, A.S. Rao, N. Singh, Optik 242 (2021) 167275.
[114] V. Singh, S. Kaur, A.S. Rao, N. Singh, Optik 226 (2021) 165927.
[115] V. Singh, S. Mahamuda, A.S. Rao, N. Singh, J.L. Rao, M. Irfan, Optik 207 (2020).
[116] V. Singh, A. Prasad, S. Kaur, A.S. Rao, N. Singh, Optik 241 (2021) 167267.
[117] K. Upadhyay, S. Thomas, R.K. Tamrakar, N. Kalarikkal, Chem. Pap. 75 (2021) 3073–3079.
[118] V. Singh, N. Singh, S. Watanabe, T.K. Gundu Rao, M.S. Pathak, A.K. Srivastava, P. K. Singh, S.J. Dhoble, J. Electron. Mater. 46 (2017) 1943–1947.
[119] V. Singh, G. Sivaramaiah, J.L. Rao, S.H. Kim, J. Lumin 157 (2015) 82–87.
[120] N. Singh, G. Sivaramaiah, J.L. Rao, S. Watanabe, T.K.G. Rao, R.V. Patel, V. Singh, J. Lumin 188 (2017) 423–428.
[121] V. Singh, K. Swapna, S. Kaur, A.S. Rao, J.L. Rao, J. Electron. Mater. 49 (2020) 3025–3030.
[122] V. Singh, G. Sivaramaiah, N. Singh, M. Mohapatra, D.A. Hakeem, M.S. Pathak, J. L. Rao, J. Mater. Sci. -Mater. Electron. 29 (2018) 944–951.
[123] S. Tamboli, R.M. Kadam, S.J. Dhoble, Luminescence 31 (2016) 1321–1328.
[124] X. Wang, Y. Chen, P.A. Kner, Z. Pan, Dalton Trans. 50 (2021) 3499–3505.
[125] S.L. Cates, E.L. Cates, M. Cho, J.-H. Kim, Environ. Sci. Technol. 48 (2014) 2290–2297.
[126] X. Xu, Z. Xiao, Y. Wang, Y. Yan, J. Shen, Y. Nie, W. You, D. Wu, L. Han, F. Lai, Opt. Mater. 134 (2022) 113191.
[127] S. Yan, Y. Liang, Y. Chen, J. Liu, D. Chen, Z. Pan, Dalton Trans. 50 (2021) 8457–8466.
[128] Z. Yin, P. Yuan, Z. Zhu, T. Li, Y. Yang, Ceram. Int. 47 (2021) 4858–4863.
[129] S. Yan, Y. Liang, Y. Zhang, B. Lou, J. Liu, D. Chen, S. Miao, C. Ma, J. Mater. Chem. C. 10 (2022) 17343–17352.
[130] X. Zhou, J. Qiao, Y. Zhao, K. Han, Z. Xia, Sci. China Mater. 65 (2021) 1103–1111.
[131] W. Yuan, T. Tan, H. Wu, R. Pang, S. Zhang, L. Jiang, D. Li, Z. Wu, C. Li, H. Zhang, J. Mater. Chem. C. 9 (2021) 5206–5216.
[132] H. Li, Q. Liu, J.-P. Ma, Z.-Y. Feng, J.-D. Liu, Q. Zhao, Y. Kuroiwa, C. Moriyoshi, B.-J. Ye, J.-Y. Zhang, C.-K. Duan, H.-T. Sun, Adv. Opt. Mater. 8 (2020) 1901727.
[133] Y. Hu, Y. Li, P. Yuan, T. Li, Y. Yang, J. Chin. Soc. Rare Earths 37 (2019) 298–302.
[134] Y.-M. Yang, Z.-Y. Li, J.-Y. Zhang, Y. Lu, S.-Q. Guo, Q. Zhao, X. Wang, Z.-J. Yong, H. Li, J.-P. Ma, Y. Kuroiwa, C. Moriyoshi, L.-L. Hu, L.-Y. Zhang, L.-R. Zheng, H.-T. Sun, Light.: Sci. Appl. 7 (2018) 88.
[135] C. Wang, M. Deng, Y. Tang, T. Sun, M. Wang, J. Wang, Z. Zhou, J. Wang, J. Phys. Chem. Lett. 14 (2023) 6386–6394.
[136] A. Antuzevics, G. Doke, G. Krieke, P. Rodionovs, D. Nilova, J. Cirulis, A. Fedotovs, U. Rogulis, Materials 16 (2023) 1776.
[137] S. Yan, Y. Liang, J. Liu, D. Chen, S. Miao, J. Bi, K. Sun, J. Mater. Chem. C. 9 (2021) 14730–14739.
[138] C.-L. Sun, J.-F. Li, C.-H. Hu, Z.-K. Jiang, Chin. Phys. Lett. 23 (2006) 1915.
[139] P. Shao, P. Xiong, Y. Xiao, Q. Chen, Y. Sun, N. Yan, D. Chen, Z. Yang, J. Mater. Chem. C. 10 (2022) 16670–16678.
[140] Q. Liu, Z.-Y. Feng, H. Li, Q. Zhao, N. Shirahata, Y. Kuroiwa, C. Moriyoshi, C.-K. Duan, H.-T. Sun, Adv. Opt. Mater. 9 (2021) 2002065.
[141] T. Lyu, P. Dorenbos, J. Mater. Chem. C. 6 (2018) 6240–6249.
[142] C.-H. Huang, T.-M. Chen, B.-M. Cheng, Inorg. Chem. 50 (2011) 6552–6556.
[143] V.P. Dotsenko, N.P. Efryushina, I.V. Berezovskaya, Mater. Lett. 28 (1996) 517–520.
[144] L. Liu, J. Shi, Y. Li, S. Peng, H. Zhong, L. Song, Y. Zhang, Chem. Eng. J. 430 (2022) 132884.
[145] H. Li, R. Pang, L. Jiang, D. Li, S. Zhang, H. Zhang, Inorg. Chem. 62 (2023) 11645–11653.
[146] H. Zhong, L. Liu, S. Peng, J. Shi, X. Sun, Y. Zhang, J. Lumin 251 (2022) 119103.
[147] S. Miao, Y. Liang, D. Chen, S. Yan, J. Liu, W. Wang, J. Bi, J. Mater. Chem. C. 10 (2022) 14211–14219.
[148] L. Liu, S. Peng, P. Lin, R. Wang, H. Zhong, X. Sun, L. Song, J. Shi, Y. Zhang, Inorg. Chem. Front. 9 (2022) 4433–4441.
[149] C. Wang, Y. Jin, J. Zhang, X. Li, H. Wu, R. Zhang, Q. Yao, Y. Hu, Chem. Eng. J. 453 (2023) 139558.
[150] J. Liu, Y. Liang, S. Yan, D. Chen, S. Miao, W. Wang, Dalton Trans. 50 (2021) 15413–15421.
[151] C. Wang, Y. Jin, R. Zhang, L. Yuan, Z. Li, H. Wu, L. Chen, Y. Hu, J. Alloy. Compd. 902 (2022) 163776.
[152] X. Li, X. Zhao, C. Wang, F. Liu, X.-j Wang, J. Lumin 248 (2022) 118932.
[153] J. Liu, Y. Liang, S. Yan, D. Chen, S. Miao, W. Wang, J. Bi, J. Mater. Chem. C. 9 (2021) 9692–9701.

[154] M. Baran, A. Kissabekova, A. Krasnikov, V. Tsiumra, L. Vasylechko, S. Zazubovich, Y. Zhydachevskyy, Opt. Mater. 137 (2023) 113584.
[155] J. Zhang, Z. Wang, Y. Zhu, X. Huo, Y. Wang, H. Suo, L. Li, P. Li, J. Mater. Chem. C. 11 (2023) 8892–8902.
[156] M. Baran, A. Kissabekova, A. Krasnikov, A. Reszka, L. Vasylechko, S. Zazubovich, Y. Zhydachevskyy, J. Lumin 253 (2023) 119483.
[157] J. Shi, X. Sun, S. Zheng, X. Fu, Y. Yang, J. Wang, H. Zhang, Adv. Opt. Mater. 7 (2019) 1900526.
[158] X. Yin, H. Zhong, L. Liu, J. Shi, X. Sun, Y. Zhang, J. Rare Earths (2023).
[159] Z. Zhou, P. Xiong, H. Liu, M. Peng, Inorg. Chem. 59 (2020) 12920–12927.
[160] T. Lyu, P. Dorenbos, Chem. Mater. 32 (2020) 1192–1209.
[161] L. Liu, K. Yu, L. Ming, Y. Sheng, S. Zheng, L. Song, J. Shi, Y. Zhang, J. Rare Earths 40 (2022) 1424–1431.
[162] L. Liu, S. Peng, Y. Guo, Y. Lin, X. Sun, L. Song, J. Shi, Y. Zhang, ACS Appl. Mater. Interfaces 14 (2022) 41215–41224.
[163] Y. Xia, F. Huang, W. Wang, A. Wang, J. Shi, J. Alloy. Compd. 476 (2009) 534–538.
[164] S. Lai, Z. Yang, J. Liao, J. Qiu, Z. Song, Y. Yang, D. Zhou, Mater. Res. Bull. 60 (2014) 714–718.
[165] A.M. Srivastava, H.A. Comanzo, Opt. Mater. 63 (2017) 118–121.
[166] B.-M. Liu, W.-J. Gan, S.-Q. Lou, R. Zou, Q. Tang, C.-X. Wang, J. Jiao, J. Wang, J. Appl. Phys. 129 (2021) 120901.
[167] D.R. Taikar, S.J. Dhoble, Optik 261 (2022) 169215.
[168] J.W. Gilliland, J. Lumin 4 (1971) 345–356.
[169] Q. Wang, X. Wu, S. Wei, Y. Wu, X. Mu, Z. Zhao, M. Wen, H. Dong, X. Zhang, F. Wu, Z. Mu, J. Lumin 225 (2020) 117353.
[170] S.K. Sharma, M. Bettinelli, I. Carrasco, J. Beyer, R. Gloaguen, J. Heitmann, J. Phys. Chem. C. 123 (2019) 14639–14646.
[171] X. Wang, P. Li, S. Zheng, J. Shi, X. Fu, H. Zhang, J. Alloy. Compd. 863 (2021) 158062.
[172] Y. Liang, F. Liu, Y. Chen, K. Sun, Z. Pan, Dalton Trans. 45 (2016) 1322–1326.
[173] E. Erdoğmuş, E. Yildiz, J. Appl. Spectrosc. 87 (2020) 615–620.
[174] E. Yıldız, E. Erdoğmuş, J. Lumin 204 (2018) 1–4.
[175] M. Xie, H. Wei, W. Wu, Inorg. Chem. 58 (2019) 1877–1885.
[176] L. Shirmane, V. Pankratov, Phys. Status Solidi (RRL) – Rapid Res. Lett. 10 (2016) 475–479.
[177] H.F. Folkerts, M.A. Hamstra, G. Blasse, Chem. Phys. Lett. 246 (1995) 135–138.
[178] A.O. Chauhan, K.A. Koparkar, N.S. Bajaj, S.K. Omanwar, AIP Conf. Proc. 1728 (2016).
[179] A. Mergen, İ. Pekgözlü, J. Lumin 134 (2013) 220–223.
[180] İ. Pekgözlü, H. Karabulut, Inorg. Mater. 45 (2009) 61–64.
[181] İ. Pekgözlü, E. Erdoğmuş, B. Demirel, M. Sabri Gök, H. Karabulut, A.S. Başak, J. Lumin 131 (2011) 2290–2293.
[182] İ. Pekgözlü, Optik 126 (2015) 1369–1371.
[183] A.B. Gawande, R.P. Sonekar, S.K. Omanwar, J. Lumin 149 (2014) 200–203.
[184] N. Fifere, A. Airinei, D. Timpu, A. Rotaru, L. Sacarescu, L. Ursu, J. Alloy. Compd. 757 (2018) 60–69.
[185] Y. Gong, Y. Liang, S. Liu, H. Li, Y. Bi, Q. Wang, Y. Dou, Inorg. Chem. Front. 8 (2021) 3760–3766.
[186] K.A. Gedekar, S.P. Wankhede, S.V. Moharil, J. Sol. -Gel Sci. Technol. 82 (2017) 344–351.
[187] V. Singh, N. Singh, V. Dubey, P.K. Singh, K.N. Shinde, V.V. Ravi Kanth Kumar, Optik 158 (2018) 1234–1239.
[188] A.O. Chauhan, C.B. Palan, N.S. Sawala, S.K. Omanwar, J. Mater. Sci.: Mater. Electron. 28 (2017) 7643–7649.
[189] H.-W. Wei, L.-M. Shao, H. Jiao, X.-P. Jing, Opt. Mater. 75 (2018) 442–447.
[190] S. Panda, P. Vinodkumar, U. Madhusoodanan, B.S. Panigrahi, Luminescence 34 (2019) 887–894.
[191] S. Liao, W. Zhang, J. Zhang, Ceram. Int. 44 (2018) 18413–18419.
[192] J. Joseph, A.A. Anappara, N. J. Chem. 40 (2016) 8110–8117.
[193] J. Shao, S. Zhu, H. Liu, Y. Song, S. Tao, B. Yang, Adv. Sci. 4 (2017) 1700395.
[194] Y. Yang, Y. Zheng, W. Cao, A. Titov, J. Hyvonen, J.R. Manders, J. Xue, P. H. Holloway, L. Qian, Nat. Photonics 9 (2015) 259–266.
[195] J. Hu, Y. Sun, X. Geng, J. Wang, Y. Guo, L. Qu, K. Zhang, Z. Li, Light.: Sci. Appl. 11 (2022) 185.
[196] W. Ye, H. Ma, H. Shi, H. Wang, A. Lv, L. Bian, M. Zhang, C. Ma, K. Ling, M. Gu, Y. Mao, X. Yao, C. Gao, K. Shen, W. Jia, J. Zhi, S. Cai, Z. Song, J. Li, Y. Zhang, S. Lu, K. Liu, C. Dong, Q. Wang, Y. Zhou, W. Yao, Y. Zhang, H. Zhang, Z. Zhang, X. Hang, Z. An, X. Liu, W. Huang, Nat. Mater. 20 (2021) 1539–1544.
[197] J. Ye, Z. Li, D.J. Kubicki, Y. Zhang, L. Dai, C. Otero-Martínez, M.A. Reus, R. Arul, K.R. Dudipala, Z. Andaji-Garmaroudi, Y.-T. Huang, Z. Li, Z. Chen, P. Müller-Buschbaum, H.-L. Yip, S.D. Stranks, C.P. Grey, J.J. Baumberg, N.C. Greenham, L. Polavarapu, A. Rao, R.L.Z. Hoye, J. Am. Chem. Soc. 144 (2022) 12102–12115.
[198] Q.A. Akkerman, S. Park, E. Radicchi, F. Nunzi, E. Mosconi, F. De Angelis, R. Brescia, P. Rastogi, M. Prato, L. Manna, Nano Lett. 17 (2017) 1924–1930.
[199] J. Xu, L. Liu, ChemNanoMat 7 (2021) 651–657.
[200] Q.A. Akkerman, V. D'Innocenzo, S. Accornero, A. Scarpellini, A. Petrozza, M. Prato, L. Manna, J. Am. Chem. Soc. 137 (2015) 10276–10281.
[201] M. Chen, H. Hu, N. Yao, X. Yuan, Q. Zhong, M. Cao, Y. Xu, Q. Zhang, J. Mater. Chem. C. 7 (2019) 14493–14498.
[202] X. Shen, S. Wang, X. Zhang, H. Wang, X. Zhang, C. Wang, Y. Gao, Z. Shi, W.W. Yu, Y. Zhang, Nanoscale 11 (2019) 11464–11469.
[203] D. Zhang, M. Yu, Y. Xu, D. Li, Y. Huang, C. Yu, C. Tang, J. Lin, Opt. Mater. 127 (2022) 112257.
[204] P. Arunkumar, H.B. Cho, K.H. Gil, S. Unithrattil, Y.H. Kim, W. Bin Im, Nat. Commun. 9 (2018) 4691.
[205] S. Sun, M. Lu, X. Gao, Z. Shi, X. Bai, W.W. Yu, Y. Zhang, Advanced, Science 8 (2021) 2102689.
[206] W. Zhang, J. Wei, Z. Gong, P. Huang, J. Xu, R. Li, S. Yu, X. Cheng, W. Zheng, X. Chen, Adv. Sci. 7 (2020) 2002210.
[207] M. Nikl, E. Mihokova, K. Nitsch, Solid State Commun. 84 (1992) 1089–1092.
[208] D. Han, J. Wang, L. Agosta, Z. Zang, B. Zhao, L. Kong, H. Lu, I. Mosquera-Lois, V. Carnevali, J. Dong, J. Zhou, H. Ji, L. Pfeifer, S.M. Zakeeruddin, Y. Yang, B. Wu, U. Rothlisberger, X. Yang, M. Grätzel, N. Wang, Nature 622 (2023) 493–498.
[209] W. Yang, P. Dang, G. Zhang, H. Lian, G. Li, J. Lin, Inorg. Chem. 61 (2022) 5903–5911.
[210] R. Zeng, K. Bai, Q. Wei, T. Chang, J. Yan, B. Ke, J. Huang, L. Wang, W. Zhou, S. Cao, J. Zhao, B. Zou, Nano Res. 14 (2021) 1551–1558.
[211] Y. Chen, L. Zhou, S. Zhou, D. You, H. Xiong, Y. Hu, Q. Chen, R. He, M. Li, Inorg. Chem. 62 (2023) 2806–2816.
[212] C. Sun, K. Jiang, M.-F. Han, M.-J. Liu, X.-K. Lian, Y.-X. Jiang, H.-S. Shi, C.-Y. Yue, X.-W. Lei, J. Mater. Chem. C. 8 (2020) 11890–11895.
[213] M. Leng, Y. Yang, K. Zeng, Z. Chen, Z. Tan, S. Li, J. Li, B. Xu, D. Li, M. P. Hautzinger, Y. Fu, T. Zhai, L. Xu, G. Niu, S. Jin, J. Tang, Adv. Funct. Mater. 28 (2018) 1704446.
[214] T. Luo, J. Wei, Mater. Chem. Phys. 253 (2020) 123374.
[215] P.H. Hart, S. Gorman, J.J. Finlay-Jones, Nat. Rev. Immunol. 11 (2011) 584–596.
[216] H.J. Vreman, R.J. Wong, D.K. Stevenson, R.K. Route, S.D. Reader, M.M. Fejer, R. Gale, D.S. Seidman, Pediatr. Res. 44 (1998) 804–809.
[217] W. Zou, A. González, D. Jampaiah, R. Ramanathan, M. Taha, S. Walia, S. Sriram, M. Bhaskaran, J.M. Dominguez-Vera, V. Bansal, Nat. Commun. 9 (2018) 3743.
[218] J.Y. Hong, J. Ahn, S. Won, S.M. Kim, Y.A. Cho, C.Y. Kim, J.Y. Sung, D.-A. Yu, Y. W. Lee, Y.B. Choe, Sci. Rep. 12 (2022) 20690.
[219] T.-R. Kwon, S.-E. Lee, J.H. Kim, Y.N. Jang, S.-Y. Kim, S.K. Mun, C.W. Kim, J. Na, B.J. Kim, Photochem. Photobiol. Sci. 19 (2020) 1009–1021.
[220] R. Dummer, M.H. Vermeer, J.J. Scarisbrick, Y.H. Kim, C. Stonesifer, C.P. Tensen, L.J. Geskin, P. Quaglino, E. Ramelyte, Nat. Rev. Dis. Prim. 7 (2021) 61.
[221] L. George, D. Peter, M. Chopra, B. George, A. Abraham, V. Mathews, A. Srivastava, S.A. Pulimood, Bone Marrow Transplant. 51 (2016) 988–990.
[222] P.S. Hemne, R.G. Kunghatkar, S.J. Dhoble, S.V. Moharil, V. Singh, Luminescence 32 (2017) 260–270.
[223] T. Zheng, M. Sójka, P. Woźny, I.R. Martín, V. Lavín, E. Zych, S. Lis, P. Du, L. Luo, M. Runowski, Adv. Opt. Mater. 10 (2022) 2201055.
[224] I. Mehta, H.-Y. Hsueh, S. Taghipour, W. Li, S. Saeedi, Robot. Auton. Syst. 161 (2023) 104332.
[225] M. Kneissl, T.-Y. Seong, J. Han, H. Amano, Nat. Photonics 13 (2019) 233–244.
[226] T. Minamikawa, T. Koma, A. Suzuki, T. Mizuno, K. Nagamatsu, H. Arimochi, K. Tsuchiya, K. Matsuoka, T. Yasui, K. Yasutomo, M. Nomaguchi, Sci. Rep. 11 (2021) 5070.
[227] C.S. Heilingloh, U.W. Aufderhorst, L. Schipper, U. Dittmer, O. Witzke, D. Yang, X. Zheng, K. Sutter, M. Trilling, M. Alt, E. Steinmann, A. Krawczyk, Am. J. Infect. Control 48 (2020) 1273–1275.
[228] H. Inagaki, A. Saito, H. Sugiyama, T. Okabayashi, S. Fujimoto, Emerg. Microbes Infect. 9 (2020) 1744–1747.
[229] N. Storm, L.G.A. McKay, S.N. Downs, R.I. Johnson, D. Birru, M. de Samber, W. Willaert, G. Cennini, A. Griffiths, Sci. Rep. 10 (2020) 22421.
[230] M. Buonanno, D. Welch, I. Shuryak, D.J. Brenner, Sci. Rep. 10 (2020) 10285.
[231] H.X. Ren Hui, J. Xiamen Univ. (Nat. Sci.) 60 (2021) 107784.
[232] A. Yadav, D. Singh, M. Lingwan, P. Yadukrishnan, S.K. Masakapalli, S. Datta, J. Integr. Plant Biol. 62 (2020) 1270–1292.
[233] T. Matthew Robson, P.J. Aphalo, A.K. Banaś, P.W. Barnes, C.C. Brelsford, G. I. Jenkins, T.K. Kotilainen, J. Łabuz, J. Martínez-Abaigar, L.O. Morales, S. Neugart, M. Pieristè, N. Rai, F. Vandenbussche, M.A.K. Jansen, Photochem. Photobiol. Sci. 18 (2019) 970–988.
[234] P. Meyer, B. Van de Poel, B. De Coninck, Hortic. Res. 8 (2021) 194.
[235] J. Li, A. Scarano, N.M. Gonzalez, F. D'Orso, Y. Yue, K. Nemeth, G. Saalbach, L. Hill, C. de Oliveira Martins, R. Moran, A. Santino, C. Martin, Nat. Plants 8 (2022) 611–616.
[236] J. Méndez-Ramos, J.C. Ruiz-Morales, P. Acosta-Mora, N.M. Khaidukov, J. Mater. Chem. C. 4 (2016) 801–806.
[237] G. Goti, K. Manal, J. Sivaguru, L. Dell'Amico, Nat. Chem. (2024), https://doi.org/10.1038/s41557-024-01472-6.
[238] Z. Liu, Y. Ding, C.Z.Y. Meng, J. Tang, Q. Qiu, Ceram. Int. 44 (2018) 14712–14716.
[239] Y. Mei, H. Xu, J. Zhang, Z. Ci, M. Duan, S. Peng, Z. Zhang, W. Tian, Y. Lu, Y. Wang, J. Alloy. Compd. 622 (2015) 908–912.
[240] H. Li, Y. Yao, X. Yang, X. Zhou, R. Lei, S. He, Environ. Sci. Pollut. Res. 29 (2022) 68293–68305.
[241] H.L. So, W. Chu, W. Xu, J. Environ. Chem. Eng. 9 (2021) 105076.
[242] A. Fakharuddin, M.K. Gangishetty, M. Abdi-Jalebi, S.-H. Chin, A.R. bin Mohd Yusoff, D.N. Congreve, W. Tress, F. Deschler, M. Vasilopoulou, H.J. Bolink, Nat. Electron. 5 (2022) 203–216.
[243] E.M. Chan, Chem. Soc. Rev. 44 (2015) 1653–1679.
[244] H. Tao, T. Wu, M. Aldeghi, T.C. Wu, A. Aspuru-Guzik, E. Kumacheva, Nat. Rev. Mater. 6 (2021) 701–716.

Junfeng Chen is currently the deputy leader of the research group of Advanced Radiation Detection Crystals and Devices at the New Materials R&D Center of Shanghai Institute of Ceramics, Chinese Academy of Sciences. He received BS degree from Zhengzhou University in 2003, and MS and Ph.D. degrees from the Shanghai Institute of Ceramics, Chinese Academy of Sciences. He visited the High Energy Physics Research Group of Caltech (Ren-Yuan Zhu Laboratory) from February to August 2016. He has been engaged in the composition-structure-defect-mechanism-engineering research of advanced scintillators, and has developed a series of crystals, arrays, detector devices and spectrometers, such as BGO, BaF_2, BaF_2:Y, CsI:Tl, and SrI_2:Eu, which are applied to nuclear medical imaging equipment (PET/CT, brain PET and SPECT, etc).

Qian Liu is a Full Professor at the Shanghai Institute of Ceramics, Chinese Academy of Sciences. She received BS and MS degrees from the Tianjin University in 1982 and 1987, respectively, and a Ph.D. degree from the Shanghai Institute of Ceramics, Chinese Academy of Sciences in 1994. Her research interests are the application of high-throughput technology for the rapid discovery of new materials including luminescent materials, dielectric materials, steel materials, etc.